White Matter Changes in the Perforant Path in ALS: Providing Evidence for ALS as a Multisystem Disease

M. Hiemstra[1], J. Mollink[1,2], M. Pallabage-Gamarallage[3], I.N. Huszar[2], K.L. Miller[2], M. Jenkinson[2], O. Ansorge[3], A.M. van Cappellen van Walsum[1]

[1] *Department of Anatomy, Donders Institute for Brain, Cognition and Behaviour, Radboud University Medical Centre, Nijmegen, Netherlands.*
[2] *FMRIB, Wellcome Centre for Integrative NeuroImaging, Oxford, United Kingdom.*
[3] *Department of Neuropathology, John Radcliffe Hospital, Oxford, United Kingdom.*

Amyotrophic lateral sclerosis (ALS) is a severe, progressive and incurable motor disease. Roughly 20% of the ALS patients are affected by a level of cognitive decline that meets the criteria for behavioural frontotemporal lobe dementia (bvFTD). ALS and bvFTD share some clinical and pathological features, for example, the deposition of TAR DNA binding protein 43(pTDP-43) in several brain regions that are part of the circuit of Papez. Previous literature suggests involvement of the perforant path, a white matter tract in the hippocampus that is part of the circuit of Papez, in patients with both ALS and bvFTD. We hypothesize that white matter degeneration in the perforant pathway is a key feature of ALS, providing a neuronal correlate for ALS as a multisystem disorder. To verify our hypothesis we studied white matter changes in ex-vivo hippocampal blocks from patients with known ALS (n=13) and controls (n=5) using diffusion MRI. The dMRI results were evaluated using polarised light imaging (PLI), a microscopy technique sensitive to density and orientation of myelinated axons. From the same hippocampal blocks, sections were cut and stained for myelin, pTDP-43, neurofilaments and activated microglia. The dMRI results show a significant decrease in fractional anisotropy (*p*=0.018) and an increase in mean diffusivity (*p*=0.0017), axial diffusivity (*p*=0.023) and radial diffusivity (*p*=0.028) in the perforant path in ALS patients compared to controls, likely indicating a loss of fibres. The PLI retardance values within the perforant path were lower in ALS cases compared to controls, however, not significantly (*p*=0.16). The retardance correlates with the fractional anisotropy (*p*=0.04). Furthermore, an increase in dispersion was observed in ALS specimens (*p*=0.04), implying a less organised axonal structure. Histology data showed a non-significant increase in myelin (PLP) (*p*=0.11) and an increase in neurofilaments (SMI-312) (*p*=0.03) in ALS cases compared to controls. No differences were found in the amount of inflammation and two out of the 13 ALS cases exhibited pTDP-43 pathology in the hippocampus. These results demonstrate degradation of the perforant path in ALS patients, providing a potential neuronal correlate for the cognitive symptoms observed in ALS and substantiating the hypothesis that ALS and bvFTD are part of the same spectrum of diseases. Future research should focus on correlating the degree of clinically observed cognitive decline to the amount of white matter atrophy in the perforant path.

Keywords: Amyotrophic Lateral Sclerosis, Frontotemporal Lobe Dementia, Perforant Pathway, Polarised Light Imaging, diffusion Magnetic Resonance Imaging

---

Corresponding author: Marlies Hiemstra; E-mail: marlieshiemstra@hotmail.com

List of abbreviations

AD	Axial diffusion
ALS	Amyotrophic lateral sclerosis
bvFTD	Behavioral Frontotemporal lobe dementia
CD68	Cluster of differentiation 68
DG	Dentate gyrus
dMRI	Diffusion magnetic resonance imaging
EC	Entorhinal cortex
FA	Fractional anisotropy
FOM-HS	Fibre orientation map hue saturation value
FOV	Field of view
LGN	Lateral geniculate nucleus
MD	Mean diffusivity
PBS	Phosphate buffered saline
PLI	Polarized light imaging
PLP	Proteolipid protein
pTDP-43	Phosphorylated TAR DNA binding protein
RD	Radial diffusion
Sub	Subicular cortices, pre-subiculum and subiculum

Introduction

Amyotrophic lateral sclerosis (ALS) is a severe, progressive and incurable motor disease that is characterized by death of motor neurons in the brain and spinal cord, resulting in a loss of voluntary movement. It is the most common form of adult onset motor neuron degeneration and has an incidence of 1-2 per 100,000 per year in the world population and about 6-7 per 100,000 in the European population (Bonafede & Mariotti, 2017; Ferrari, Kopogiannis, Huey & Momeni, 2011; Logroscino et al., 2010; Tan, Ke, Ittner & Halliday, 2017). ALS can occur both sporadically (90%) and familially (10%) and has a median survival of three years after disease onset (Tan et al., 2017). ALS has mainly been described as a neurological disorder that affects the motor system, but more and more evidence is suggesting ALS to be a multisystem neurodegenerative disease because other areas besides motor areas of the brain also undergo degeneration. One of the most prominent bodies of evidence of ALS being a multisystem disorder is that 50% of the ALS patients suffer from a form of cognitive impairment and 15% of the ALS patients are affected by a level of cognitive decline that meets the criteria for behavioural frontotemporal lobe dementia (bvFTD) (Cykowski et al., 2017). We examined the whole brains and spinal cords of 57 patients (35 men; 22 women; mean age 63.3 years; 15 patients with c9orf72-associated ALS [c9ALS]; Phukan et al., 2012; Tan et al., 2017) the population-based frequency, clinical characteristics and natural history of cognitive impairment in amyotrophic lateral sclerosis (ALS). However, a clear neural correlate of these cognitive symptoms has been lacking to date. Looking into the resemblance between bvFTD and ALS provides information about the neural substrate of the cognitive problems observed in ALS.

Frontotemporal dementia (FTD) is a heterogeneous form of dementia that is characterized by progressive neurodegeneration in the temporal and frontal lobes. Different symptoms can prevail in FTD, resulting in three different subtypes: bvFTD, semantic FTD and progressive non-fluent FTD (Gao, Almeida, 2017; Ghosh & Lippa, 2015; Warren et al., 2013).

ALS and bvFTD share neuropathological, genetic and clinical features providing lending to the hypothesis that bvFTD and ALS are part of the same spectrum of diseases and providing further evidence for ALS being a multisystem disorder (Ferrari et al., 2011). The strongest neuropathological resemblance between ALS and bvFTD pathology is the deposition of ubiquitinated and hyperphosphorylated TAR DNA binding protein 43 (pTDP-43) in select neurons and glial cells of the central nervous system (Ferrari et al., 2011; Scotter, Chen & Shaw 2015). Normal TAR DNA binding protein 43(TDP-43) is mainly located in the cell-nucleus where it plays a role in inhibition of splicing and in exon skipping. In ALS and FTD pTDP-43 is mainly located in the cytoplasm where it forms potentially neurotoxic aggregations (Hu & Grossman, 2009; Mackenzie & Rademakers, 2008). In ALS, pTDP-43 pathology is present in different brain regions and develops over time via a specific pattern. Lesions spread from the motor neurons in the brainstem and spinal cord and also from the frontal neocortex to the parietal and temporal neo- and sub-cortical regions (Brettschneider et al., 2014; Brettschneider et al., 2013).

In bvFTD sequential patterns of spreading of the pTDP-43 inclusions are also observed. In bvFTD, the inclusions spread from the orbitofrontal cortex and amygdala towards the frontal and temporal cortices before progressing to the visual cortex, motor system and cerebellum (Brettschneider et al., 2014; Tan et al., 2015).

Even though pTDP-43 is associated with both ALS and FTD, genetic screening has been controversial, leaving the question open whether mutations in TDP-43 are causal to the neuropathology of ALS/FTD. Most of the genetic variability that is related to TDP-43, like mutations in the TARDBP gene that encodes for TDP-43, seems to be related to ALS cases (Sreedharan et al., 2008). To date there is hardly any evidence of mutations in TDP-43 associated with either FTD or ALS. Nevertheless, some genetic overlap between FTD and ALS can be found in other genes. For example, in both diseases mutations in the C9ORF2 gene and mutations in progranuline gene (PGRN) seem to play a role (Gao, Almeida, 2017; Ferrari et al., 2011).

Another resemblance between ALS and bvFTD was found in the previously mentioned areas affected by pTDP-43. Several of these cortical regions relate to each other via the Papez circuitry. The Papez circuit is a major loop of the limbic system and its main functions are the cortical control of emotion and the consolidation and retrieval of memory (Pessoa & Hof, 2015; Musio, 1997). The circuit is comprised of the hippocampal formation, mammillary bodies, fornix, anterior thalamic nucleus and the anterior cingulate (Fig. 1) (Shah, Jhawar & Goeal, 2012).

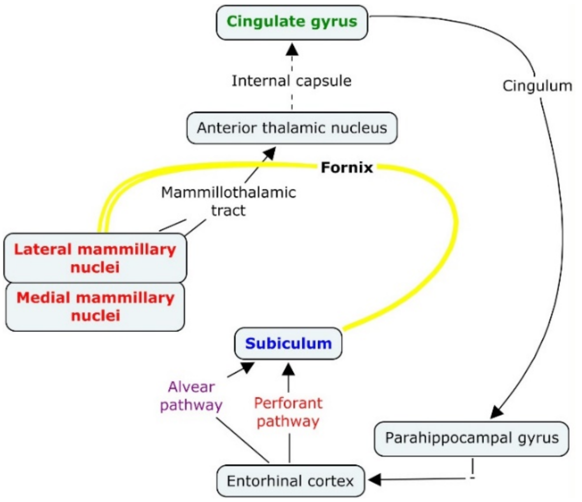

Figure 1. Schematic representation of the Papez circuit consisting of the entorhinal cortex, which projects to the subiculum via the perforant and alvear pathway. The subiculum has a projection to the mammillary nuclei via the fornix. From here the circuit continues to the cingulate gyrus via the anterior thalamic nucleus and the internal capsule. From the cingulate gyrus there is a projection to the parahippocampal gyrus via the cingulum ("figure Papez circuit," n.d.).

In vivo and post mortem MRI volumetric analyses demonstrate distinct regional grey and white matter atrophy of the Papez circuit in bvFTD (Hornberger et al., 2012; Irish et al., 2013). The main symptoms of bvFTD are functionally related to the Papez circuit since the main characteristics are progressive change in emotional regulation and changes in personality (Bott, Radke, Stephens & Kramer, 2014). Recent evidence also recognises episodic memory deficits in bvFTD, with the amount of atrophy in the Papez circuit determining the degree of episodic memory problems (Hornberger and Piguet, 2012; Hornberger et al., 2012).

Little is known about the involvement of the Papez circuitry in ALS. However, it was shown that the amount of TDP-43 pathology in ALS patients correlates with cognitive decline (Montreal Cognitive Assessment test scores), but not with the duration of the disease or its rate of progression (Brettschneider et al., 2013) brainstem motor nuclei of cranial nerves V, VII, and X-XII, and spinal cord α-motoneurons (stage 1; Cykowski et al., 2017). We examined the whole brains and spinal cords of 57 patients (35 men; 22 women; mean age 63.3 years; 15 patients with c9orf72-associated ALS [c9ALS]).

Most studies on neurodegeneration in ALS have focused on white matter areas related to motor function like the motor cortex, the corpus callosum and the corticospinal tract (Cirillo et al., 2012; Filippini et al., 2010; Horsfield & Jones, 2002; Lillo et al., 2012). To our knowledge, there are only three studies that investigated sub-cortical changes (Barbagallo et al., 2014; Thivard et al., 2007; Takeda, Uchihara, Mochizuki, Mizutani & Iwata, 2007). Two of these studies focused on grey matter integrity. An increase in mean diffusivity (MD) was found in ALS patients compared to controls in the amygdala, hippocampus and thalamus, which are part of the circuit of Papez (Barbagallo et al., 2014; Thivard et al., 2007).

The third study linked ALS to one of the projections of the circuit of Papez: the perforant path (Takeda, Uchihara, Mochizuki, Mizutani & Iwata, 2007). This path runs from the neurons in layer II and III of the entorhinal cortex (EC), through the pyramidal layer of the subiculum (Sub) to the molecular layer of the Sub, dentate gyrus (DG) and the CA3 region of the hippocampus (Fig. 2). The path is known to have an important function in memory and degeneration of this path is linked to the severe memory impairments in Alzheimer's disease (Hyman, Van Hoesen, Kromer & Damasio, 1986; Thal et al., 2000). The third ALS-related study however did not directly investigate the white matter of the perforant path, but rather evaluated the regions belonging to the path with a haematoxylin/eosin stain. Semi-quantitative analysis showed entorhinal cortex degeneration, subicular degeneration and laminar spongiosis of the DG in ALS patients. This damage, potentially caused by pTDP-43 inclusions, correlated with the degree of episodic memory deficits (Takeda, Uchihara, Mochizuki, Mizutani & Iwata, 2007). The previously mentioned white matter atrophy of the circuit of Papez in bvFTD also begins in the hippocampal area (Hornberger et al., 2012; Irish et al., 2013).

Since the perforant path seems to be affected in both ALS and dementia, we hypothesize that degeneration of the perforant path is one of the key projections to be affected in ALS, providing further evidence for ALS as a multisystem disease and providing a neural correlated for the cognitive impairments in ALS.

To verify our hypothesis, several imaging techniques were used to visualise the white matter tracts within and surrounding the hippocampus on post mortem brains of controls and of patients with ALS. First, diffusion magnetic resonance imaging (dMRI), a technique that provides 3D information about white matter tracts based on the diffusion of water within tissue (Bastiani & Roebroeck, 2015), was performed. By measuring the orientation dependence of water diffusion, an estimation of

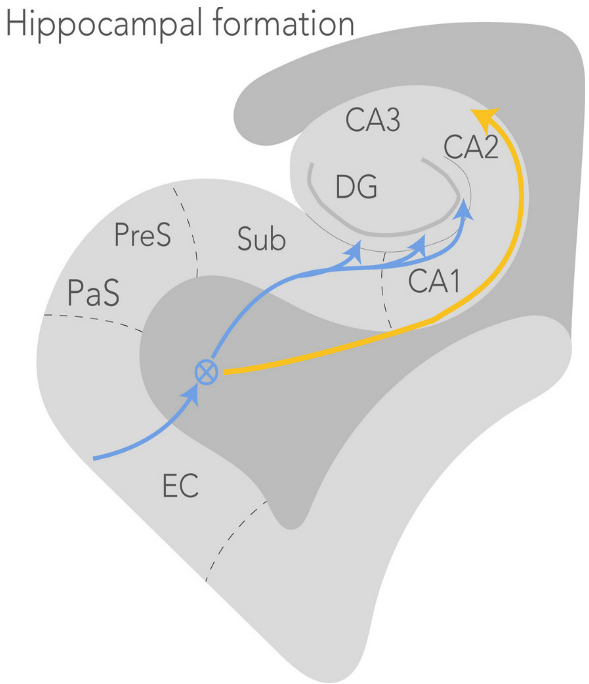

Figure 2. A schematic representation of the perforant path (blue) and the alvear path (yellow). The perforant path starts in the entorhinal cortex and projects through the subiculum via the molecular layer of the hippocampus to the dentate gyrus and the CA3 region of the hippocampus (circled-cross indicates out of screen – i.e. anterior-posterior – orientation). The alvear path projects via the CA1 region into the hippocampus. CA, cornu ammonis; DG, dentate gyrus; EC, entorhinal cortex; PaS, parasubiculum; PreS, presubiculum; Sub, subiculum.

the microstructure of the brain tissue was made (Jbabdi, Sotiropoulos, Haber, Van Essen & Behrens, 2015). dMRI has a resolution on the millimetre scale and because it is a non-invasive technique, it can be used for *in vivo* diagnostics and research (Bastiani & Roebroeck, 2015).

Second, polarised light imaging (PLI), a microscopy technique that quantifies the orientation of myelinated axons based on birefringence of myelin sheath in thin brain slices, was used. PLI is a relatively new technique and has, to our knowledge, never been used to compare properties of myelinated tracts between cases and controls. We correlated the results of PLI with the different dMRI metrics. To correlate differences in white matter with potential protein pathologies and to further complement the PLI and dMRI data, (immuno)histochemical stainings were carried out to visualise myelin, microglial activation, neurofilaments and pTDP-43 inclusions.

The aim of the research is to identify the potential changes in grey and white matter within the hippocampus in patients with ALS to further contribute to the hypothesis that ALS is a multisystem disorder and to get insight in the potential neural substrates of the cognitive deficits observed in ALS. Furthermore, our research elaborates on the hypothesis that ALS and bvFTD are part of the same spectrum of diseases.

Methods

Tissue

For this study, 13 post-mortem ALS human brains were acquired with permission from the Oxford Brain Bank at the John Radcliffe Hospital in Headington, United Kingdom. Five age matched post-mortem human control brains were acquired via the body donor program at the Department of Anatomy of the Radboud University Medical Centre, Nijmegen, The Netherlands. The human brains were removed from the skull and fixed in 2-4% formalin. Details on the history of each specimen are listed in Table 1. All brains were cut in coronal slabs of 5 mm thickness and the hippocampus was sampled in a slab comprising the lateral geniculate nucleus (LGN) as a key anatomical landmark. The hippocampal regions representing the perforant path were sampled for ALS cases (n=13, Oxford Brain Bank) and controls (n=5, Department of Anatomy, Nijmegen).

ALS classification was based on the neuropathological assessment of pTDP-43 proteinopathy in key gatekeeper regions previously defined by Tan and colleagues (Tan et al., 2015) encoded by TARDBP. pTDP-43 protein pathology was visually rated on a scale of 0 to 4 based on the rating scale of Tan and colleagues, with 0 indicating no protein pathology and 4 indicating severe pathology (Fig. 3).

Representative blocks of 13 other brain regions were sampled and stained following standard brain banking protocol for diagnostic purposes (Table 2) (Montine et al., 2012).

Magnetic resonance imaging acquisition

The imaging pipeline for all hippocampus blocks is shown in Figure 4. Out of the 18 blocks, 17 blocks were analysed with dMRI (Control n=5, ALS n=12). Prior to scanning all specimens were placed in phosphate buffered saline (PBS 0.1M pH=7.4) for at least 24 hours to reverse the decrease in T2-relaxation introduced by formalin (Shepherd, Thelwall, Stanisz & Blackcand, 2009) time-intensive MRI acquisitions without motion artifacts, such as those required

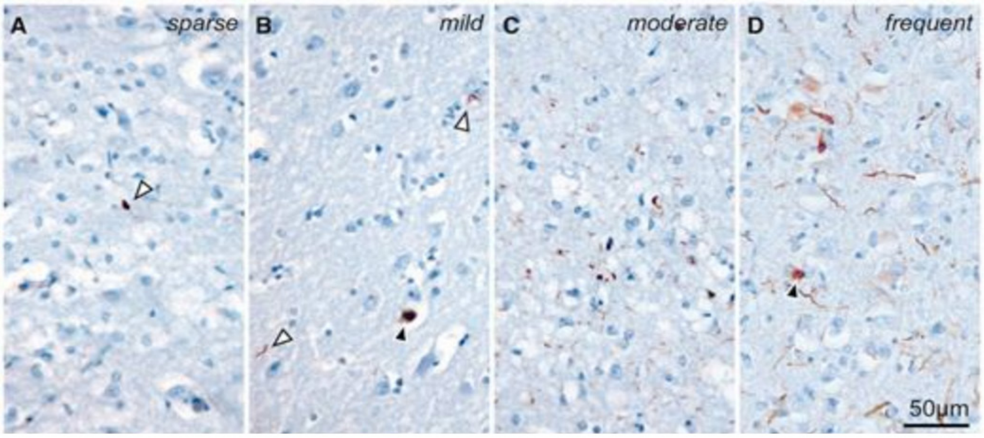

The severity of TDP-43 pathology in the anterior cingulate cortex rated on a five-point scale. 0 = no detectable pathology across the entire section (not shown), 1 = sparse (<5 inclusions across the entire section, **A**); 2 = mild (some pathology observed in most fields of view at × 100 magnification, **B**); 3 = moderate (**C**); and 4 = frequent (**D**). Solid arrowheads indicate neuronal inclusions. Open arrowheads show examples of neurites and glia.

Figure 3. Visual rating scale for pTDP-43 pathology developed by Tan et al. The anterior cingulate was stained for pTDP-43 and counterstained with haematoxylin. Pathology was rated on a scale from 0-4, with a 0 indicating no pathology, 1 indicating sparse pathology, 2 indicating mild pathology, 3 indicating moderate pathology and a 4 indicating severe pathology. Solid arrowheads indicate neuronal inclusions. Open arrowheads show examples of neurites and glia (Tan et al., 2015).

Table 1.
Post mortem specimen details from control (1-5) and ALS/ALS-FTD brains(6-18). Abbreviations: Post-mortem interval (PMI), fixation time (FT), cause of death (COD).

#	**PMI (days)**	**FT (months)**	**Sex**	**COD**	**Age**
1	0.5	12	M	Heart failure	67
2	0.5	14	M	Lungcancer	61
3	0.5	8	F	Old	82
4	0.5	8.5	M	Leukemia	73
5	1	15	F	Fluid in the lungs	71
6	4	47	F	Unknown	61
7	Unknown	Unknown	F	Unknown	77
8	3	42	M	Unknown	82
9	5	42	F	Unknown	53
10	4	39	M	Unknown	76
11	2	36	M	Unknown	78
12	1	36	F	Unknown	81
13	2	35	F	Unknown	81
14	2	26	F	Unknown	80
15	2	15	F	Infection (?), pneumonia. Difficulty with breathing.	67
16	2	14	F	Respiratory failure	74
17	4	14	M	Shortness of breath	55
18	2	13	F	Unknown	53

Table 2.
Stainings performed on 13 brain regions sampled for diagnostics, following standard brain banking protocol. Staining were performed for Alzheimer's disease (4G8 and AT8), Parkinson's disease (alpha-synuclein), ALS (TDP-43) and other general neuropathology (p62).

	HE	4G8	Alpha-synuclein	AT8	TDP-43	P62
Basal Ganglia	x	x	x			
Anterior hippo	x	x		x		
Amygdala	x	x	x	x	x	
Ant cingulate	x		x			
Mid front gyrus	x	x	x	x		x
Temp gyrus	x	x	x	x		x
Inferior parietal lobule	x	x	x	x		
Occipital gyus	x	x	x	x		
Midbrain	x	x	x			
Pons	x		x			
medulla	x		x			x
Cerebellum	x	x				x
M1/S1	x					x

for brain atlas projects, but the aldehyde fixatives used may significantly alter tissue MRI properties. To test this hypothesis, this study characterized the impact of common aldehyde fixatives on the MRI properties of a rat brain slice model. Rat cortical slices immersion-fixed in 4% formaldehyde demonstrated 21% and 81% reductions in tissue T1. For scanning, specimens were transferred to a 100 ml syringe filled with fluorinert® (Solvay Solexis Inc), a proton-free solution which is susceptibility matched to the tissue. If necessary, additional gauzes were place in the syringe to immobilize the tissue.

All scans were performed at room temperature on a 11.7T Bruker BioSpec Avance III preclinical MR system (Bruker BioSpin, Ettlingen, Germany) using a birdcage coil (Bruker Biospin). T1- and T2-weighted high-resolution structural images were obtained for anatomical reference.

T1-weighted structural images were acquired with a fast low angle shot gradient echo (FLASH) sequence at a resolution of 0.1x0.1x0.1 mm (TR=25 ms, TE= 3.4 ms, flip angle=10°). T2-weighted images were acquired with a multi-gradient echo sequence at a resolution of 0.1x0.1x0.1mm ((TR=35.813 ms, TE= 15 ms, flip angle=30°).

Diffusion weighted images were obtained using a spin-echo sequence with an EPI readout (TR=13.75s, TE= 30.066 ms, Δ= 12.5 ms, δ= 4.0). Two shells were acquired (b=2000,4000 s/mm^2), each employed at 64 gradient directions (128 in total) in addition to six images with negligible diffusion weighting (b=14s/mm^2). The specimens were covered in the coronal plane of the scanner with a field-of-view of 28.8 x 28.8 mm that was sampled with a 72 x 72 matrix. Together with a slice thickness of 0.4 mm this created isotropic voxels. The number of slices varied between 80 and 100 depending on the dimension of each specimen.

Probabilistic tractography

Processing of all MR images was performed with FSL (Woolrich et al., 2009) noisy images of the brain. This might be the inference of percent changes in blood flow in perfusion fMRI data, segmentation of subcortical structures from structural MRI, or inference of the probability of an anatomical connection between an area of cortex and a subthalamic nucleus using diffusion MRI. In this article we will describe how Bayesian techniques have made a significant impact in tackling problems such as these, particularly in regards to the analysis tools in the FMRIB Software Library (FSL). A diffusion tensor was estimated at each voxel in the dMRI data. Four different tensor metrics were derived from this diffusion tensor: the fractional anisotropy (FA), mean diffusivity (MD), axial diffusivity (AD) and the radial diffusivity (RD). The FA value is a metric describing the diffusion directionality of water ranging from 0 to 1, with a value of 0 indicating fully isotropic diffusion and 1 indicating fully anisotropic diffusion (Fig. 5). A reduction in FA may indicate white matter damage. The MD value is a measure for the total amount of diffusion, where an increase

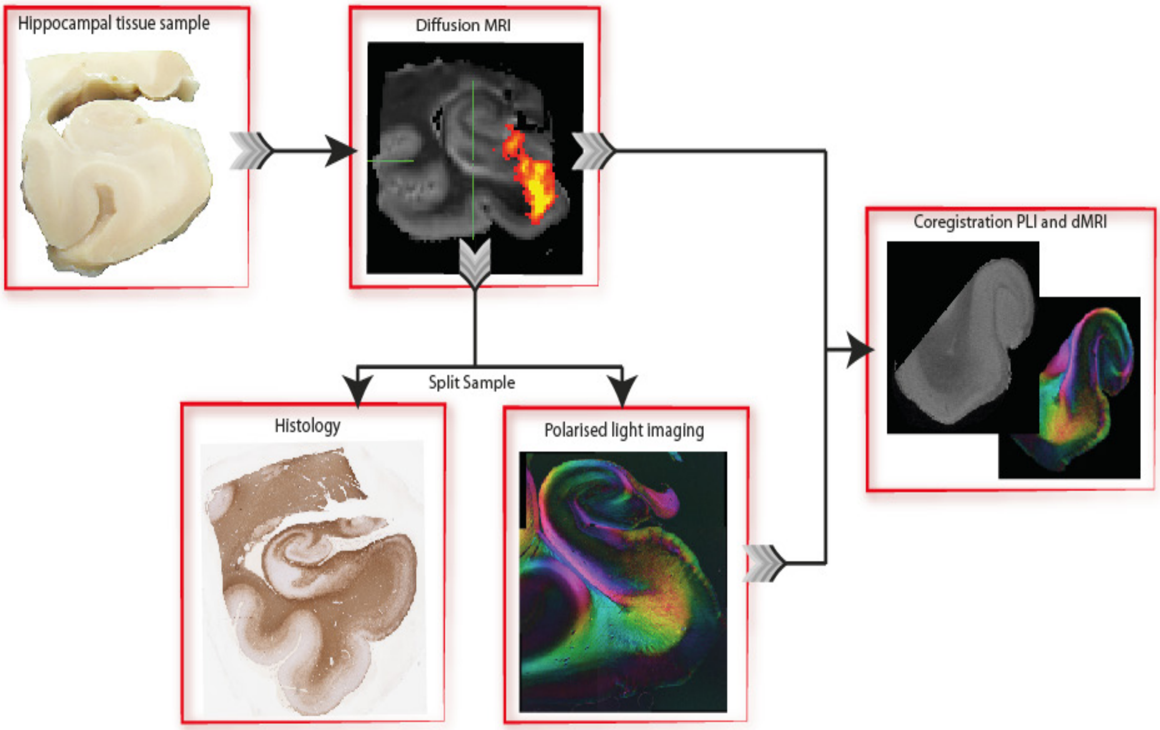

Figure 4. Processing and analysis pipeline of the specimens. All hippocampal blocks were scanned with diffusion MRI. After scanning, the blocks were bisected into two parts, one part was used for histological staining and the other part for polarized light imaging). In the end, the polarized light imaging data was co-registered with the diffusion MRI data.

in MD may also be possible marker for white matter damage. The AD is a direct indicator of the amount of the diffusion along the main diffusion axis, while the RD gives information about the diffusion along the axes parallel to the main diffusion direction. An increase in RD was previously shown to correlate with a reduction in myelin (Aung, Mar & Benzinger, 2013).

In order to extract the FA, MD, RD and AD metrics within the perforant path, probabilistic tractography was performed. To delineate the perforant path in the hippocampus specimen, tractography was run on the dMRI data. First, we estimated the fibre configuration in each voxel using the Bedpostx algorithm (Behrens et al., 2003) which was modified to handle multi-shell diffusion data (Jbabdi, Sotiropoulos, Savio, Graña & Behrens, 2012). We fitted up to three fibre orientations within each voxel depending on the level of support by the diffusion signal. Probabilistic tractography was then performed using the probtrackx2 algorithm (Behrens, Berg, Jbadbu, Rushworth & Woolrich, 2007). The (pre-)subiculum and the DG were manually segmented and served as seed and waypoints masks, respectively (Fig. 6). For each seedvoxel, we generated 5000 streamlines per voxel, only keeping those that terminate in the DG. The curvature threshold was set to 0.2 (corresponding to approximately 80°), with a step length of 0.2 and a minimal fibre volume threshold of 0.01. A loop check was performed such that pathways that looped back to themselves were excluded. After probabilistic tractography, a connection probability threshold was empirically determined and only the streamlines that followed the approximate course of the performant path were retained using exclusion masks that were determined for each slice individually. From all perforant path voxels, FA, MD, RD and AD values were extracted and averaged for each specimen separately.

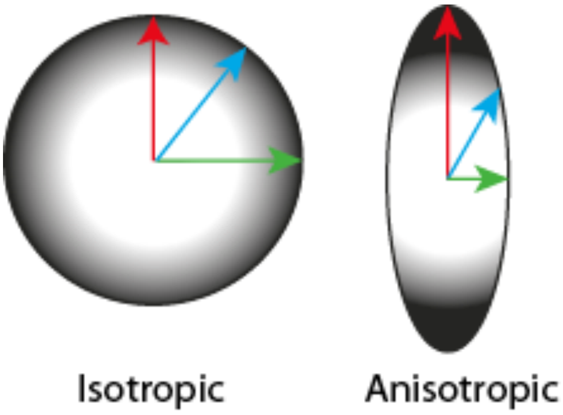

Figure 5. Isotropic diffusion (left) is associated with an FA value of 0. The more anisotropic (right) the diffusion, the higher FA value.

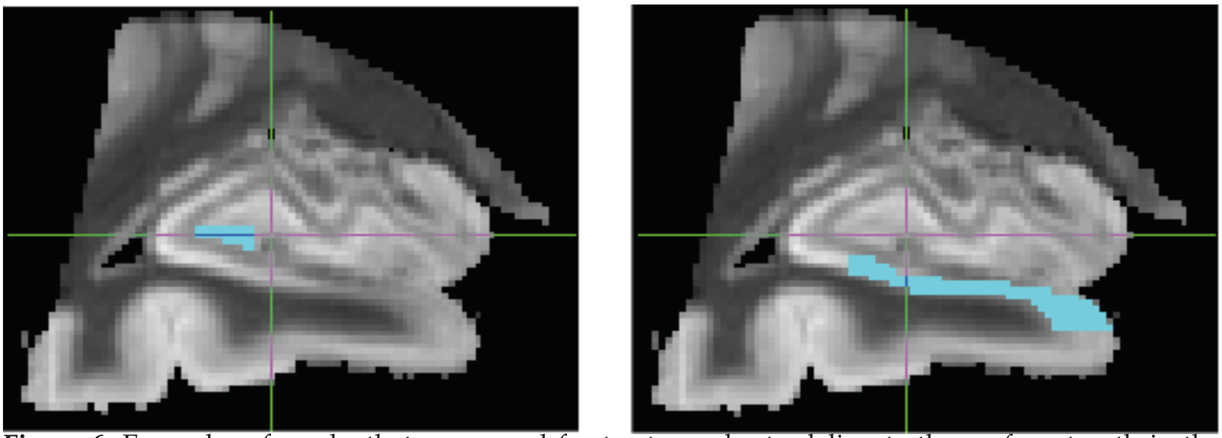

Figure 6. Examples of masks that were used for tractography to delineate the perforant path in the hippocampus. Left: The seed mask (start of tractography) for the presubiculum and subiculum. Right: The waypoint mask (end of tractography) for the dentate gyrus.

Polarized light imaging

PLI is a microscopy technique that is able to quantify the fibre orientation of myelinated axons using the birefringent property of myelin. When passing polarized light through brain tissue, the interaction of the light with the birefringent myelin results in a transmitted light intensity that depends on the angle between the myelin sheet and the polarizing filter on the microscope. The PLI raw signal consists of the transmitted light intensity at a single pixel over various polarizer orientations from which an in-plane fibre orientation can be estimated (Axer et al., 2011; Larsen, Griffin, Gräßel, Witte & Axer, 2007) the structural basis of the human connectome. In contrast to animal brains, where a multitude of tract tracing methods can be used, magnetic resonance (MR). After dMRI, all 18 hippocampal blocks were bisected along the coronal plane into two approximately equal parts. One part was embedded in paraffin for histology and the other part was frozen for PLI (Fig. 3). Frozen sections are preferred for PLI as the lipids in the myelin sheath remain preserved. After cryoprotection with 30% sucrose in PBS, all tissue blocks were sectioned at 50 µm thickness on a freezing microtome (Microm HM 440E Microtome). The sections representing the perforant path were mounted on glass slides coated with 0.5% gelatin and 0.05% potassium chrome(III) sulfatelycerin and were coverslipped with PVP, a water-soluble mounting medium.

PLI images were acquired on a Zeiss Axio Imager A2 microscope upgraded with a stationary polarizer, a quarter wave plate and a rotating polarizer. Light first passes through the stationary polarizer and a quarter wave plate positioned at a 45° angle relative to the stationary polarizer to create circularly polarized light. Once polarized, the light encounters the birefringent myelin that induces a phase shift. To capture the angular extent of this phase shift, images were acquired at 9 equiangular orientations of the rotating polarizer from 0° to 160° with a CCD camera. Together with a 1.25x magnifying objective, this yielded a spatial resolution of approximately 4 µm/pixel. Only the green channel was used for further processing as the quarter wave plate is designed for this wavelength. A set of background images was acquired for every rotation angle to correct for inhomogeneous background illumination. Background correction of the images was performed as described by Dammers and colleagues (2010). Three different parameters were derived from the raw PLI data by fitting the light intensity at each pixel to a sinusoid. The phase of the sinusoid gave the in-plane orientation, the phase shift induced to the light wave provided the retardance and the transmittance was calculated as the average amount of light passing through the tissue. The retardance and in-plane orientation maps were combined in the fibre orientation map, allowing for which visualization of the direction of myelinated fibres within the tissue (Axer et al., 2011b).

As the hippocampus sections were larger than the microscope's field-of-view (FOV), multiple FOVs were acquired to cover an entire specimen. We ensured that there was at least 10% overlap between neighbouring FOVs, such that these could be stitched together automatically. Landmarks in each FOV were described using Speed Up Robust Features (SURF) and matched together using custom written software in MATLAB (MATLAB and Statistics Toolbox Release 2017a, The MathWorks, Inc., Natick, Massachusetts, United States). A rigid transformation between the neighbouring FOVs was then computed based on the distance between the matched features. After all transformations were estimated, the individual FOVs were stitched together to reconstruct the entire specimen.

Co-registration of PLI and MRI data

In order to make an anatomically correctly match between the dMRI and PLI data, non-linear registration of PLI-derived parametric images with corresponding MRI volumes was performed. The PLI and MRI images were registered in 2 dimensions after manually selecting a slice from the MRI volume that maximised the visual correspondence of observed anatomical contours between PLI and MRI images. The segmentation mask was subsequently applied to all parametric PLI images pertaining to the same specimen. Bi-directional non-linear image registration was carried out between segmented transmittance images and segmented 2D MR images so that aligned PLI-MRI image pairs were obtained at both at the resolution of MRI and that of PLI. The obtained registration parameters were subsequently used to register other parametric PLI images with the MRI volume (Fig. 7). The registration algorithm was implemented in Python 3.6 by Istvan N. Huszar, based on the Tensor Image Registration Library (Huszar, Miller, Pallebage-Gamarallage, Ansgore, & Mirfin, 2018).

The course of image registration comprised of three steps: resizing the input image, linear registration, and non-linear registration. The input image was resampled using bilinear interpolation to match the resolution of the target image. The isotropic scaling factor was inferred from the parameters of an initial rigid-body registration between the PLI-transmittance and the MR images using the linear registration model of the second step. The linear registration step utilised a 2D affine transformation model to maximise the normalised mutual information of the images using Powell's optimisation method. In the non-linear registration step, the images were re-represented using the Modality-Independent Neighbourhood Descriptor

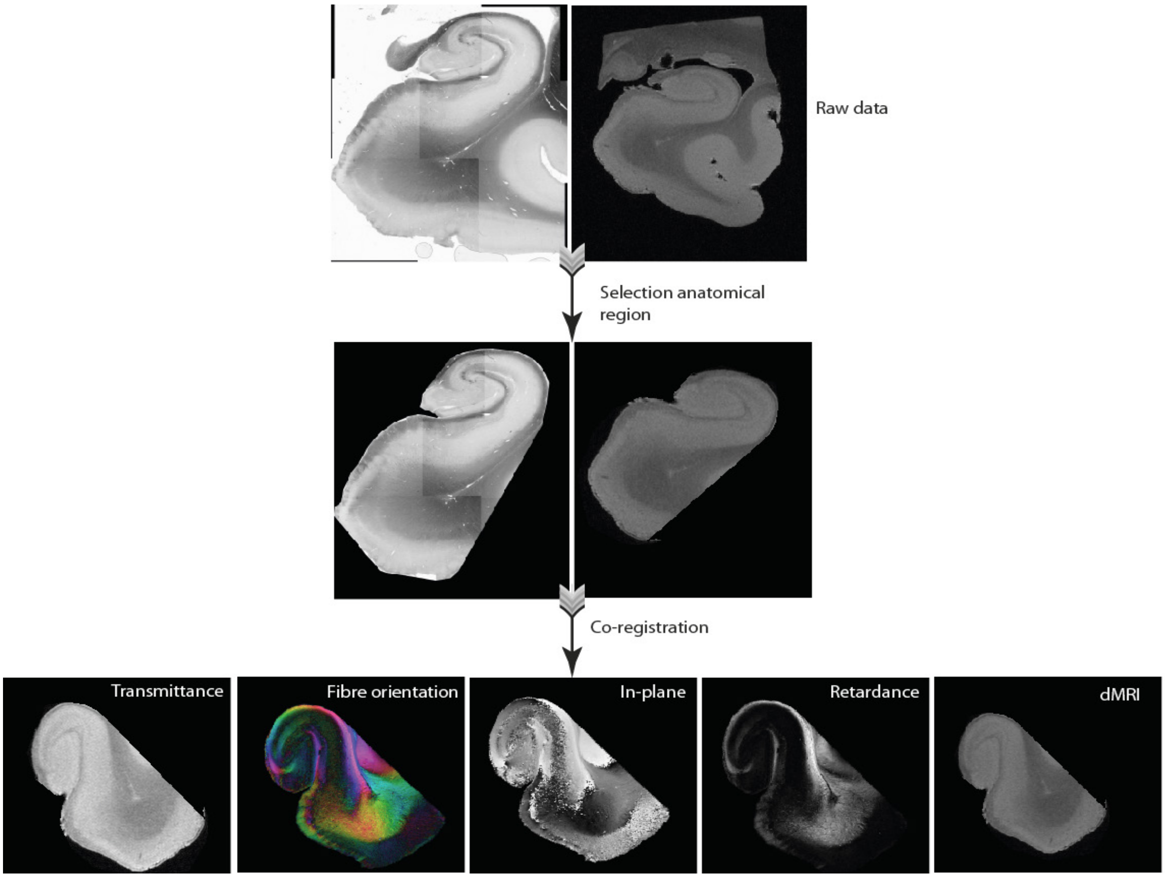

Figure 7. Example of co-registration of PLI with dMRI. On the top row, the transmittance map (left) and dMRI T1-weighted image (right) are depicted. A selection of the anatomical regions representing the perforant path was made to improve the co-registration result and the PLI selection was co-registered with the dMRI selection (middle row). The transformation that was applied to the transmittance map was also applied to the fibre orientation map, in-plane fibre orientation map and retardance map (bottom row).

(MIND) (Heinrich et al., 2012). This representation was used to calculate a cost function that was less sensitive to the differences in image contrast across the two modalities. The cost function was defined as the cumulative Euclidean distance between the image's MIND vectors, and it was minimised using Gauss-Newton optimisation for fast convergence (Heinrich et al., 2012). During the minimisation process, the input image was transformed voxel-wise, using a diffusion-regularised deformation field to ensure the smoothness of image deformation. A multi-resolution approach was adopted in both stages of the registration to avoid misalignment due to local minima in the cost functions. The image registration approach used in this study is a re-implemented and modified version of the algorithm that had been used previously by our research group to align histological images with MRI (Mollink et al., 2017). The modifications were necessary to obtain accurate spatial alignment between PLI and MRI.

Analysis of PLI data

Retardance.

In addition to fibre orientation, the retardance was derived from the PLI raw images. The retardance informs about how much the phase of the light wave is shifted due to interaction with myelin and is therefore used to evaluate the amount of myelin within a section. For one section per subject, the retardance values over the perforant path found with dMRI tractography were calculated by co-registering the PLI data with the dMRI data (Fig. 7). However, in between 8-12 PLI sections per subject were sectioned and processed. Due to time constraints, it was not possible to co-register all sections. Therefore, the other 7-11 sections were analysed by manually delineating the perforant path observed in diffusion MRI in the PLI transmittance map (supplementary Fig. 2). The retardance values under the dMRI path were extracted and averaged for all slices for each specimen to look for case-control differences.

Dispersion.

Another parameter that was extracted from the raw PLI data was the in-plane direction. The in-plane map describes the in-section direction of each fibre ranging from 0 to π. This map was used to estimate fibre dispersion. A higher degree of dispersion is associated with the beaded and fragmented fibre geometries that are associated with Wallerian axonal degeneration (Kerschensteiner, Schwab, Lichtman & Misgeld, 2005; Waller, 1850). Following a similar method to quantify the amount of dispersion from PLI fibre orientations as Mollink and colleagues (2017), a Von Mises distribution was fitted to fibre orientations in a local neighbourhood of 50x50 pixels. The Von Mises distribution is a circular normal distribution whose concentration is described by $\varkappa$ (supplementary Fig. 3). When all samples are oriented isotropic, $\varkappa = 0$ and $\varkappa$ increases when the distribution becomes more centred around one angle. Dispersion is therefore calculated as:

$$Dispersion = 1/\kappa$$

The region of interest, namely the perforant path, was manually delineated in all polarized light imaging sections based on the tractography data for each subject separately and the dispersion values within the region of interest were calculated.

Immunohistochemistry

To investigate the pTDP-43 protein pathology, microglial activation, myelination and the amount of neurofilaments, antibodies against pTDP-43, cluster of differentiation 68 (CD68), proteolipid protein (PLP) and SMI-312 were used for immunohistochemistry, respectively. All tissue blocks were embedded in paraffin and cut in 6 µm thin sections for staining for CD68, PLP and SMI312. Sections for pTDP-43 had a thickness of 10 µm. For every specimen 5 sections were stained, one for each protein. The sections were then mounted on Superfrost Plus slides (ThermoFisher, Art. No. J1800BMNZ). The sections were deparaffinised in xylene and rehydrated through a series of 100%, 100%, 90% and 70% ethanol. The endogenous peroxidase was blocked by incubating the sections 3% H_2O_2 in PBS for 30 minutes. Subsequently, antigen binding sides for pTDP-43 and CD68 were retrieved by autoclaving in citrate buffer (pH6). Antigen retrieval for PLP and SMI-312 was achieved through heating the sections submerged in citrate buffer (pH=6) in a microwave. After antigen retrieval, the sections were washed with PBS. After washing, the primary antibody was added. All primary antibodies were diluted in TBS/T (pH=7.6). The primary antibodies against PLP (mouse-anti- PLP, 1:1000, Bio-Rad, MCA839G), CD68 (mouse-anti-CD68, 1:200, Dako Denmark, M0876) and SMI-312 (Mouse-anti-SMI-312, 1:2000, BioLegend, 837901) were incubated for one hour at room temperature. The primary antibody against pTDP-43 (Mouse-anti-pTDP-43, 1:40 000, CosmoBio, PS409/410) was incubated over night at 4 °C. After washing, the secondary antibody containing HRP Rabbit/Mouse Serum (EnVision Detection Systems, Peroxidase/DAB, Rabbit/Mouse) was added and incubated for 1 hour. After washing, a DAB substrate buffer solution was added (EnVision Detection Systems, Peroxidase/DAB, Rabbit/Mouse) and incubated for 5 minutes. Sections were washed with PBS to stop the reaction. Finally, a counterstain for haematoxylin was performed to visualise the nuclei. After the counterstain sections were dehydrated and mounted with DPX.

Histological image analysis

Sections were scanned on the Aperio ScanScope AT Turbo device at a 20x magnification. All images were automatically segmented making use of great colour contrast between the DAB stain and the haematoxylin counterstain. A specific colour cluster for each structure of interest was empirically defined in HSV colour-space using MATLAB's interactive colour thresholder application (MATLAB and Statistics Toolbox Release 2017a, The MathWorks, Inc., Natick, Massachusetts, United States). The saturation and value thresholds were also optimised per stain so that the segmentations would represent the DAB-staining without much contribution of background staining. Pixels that fell within the colour segmentation were considered to be positive.

To quantify the amount of staining, a stained area fraction was calculated as the relative number of positive pixels within a local neighbourhood of 100x100 pixels. These area fraction maps were used to get an estimate of the histological structures, for example, myelin density, in a certain region of interest. The region of interest, namely, the perforant path, was manually drawn in all histological sections based on the tractography data, for each subject and stain separately (Fig. 12A).

Statistics

All statistical analyses were performed with IBM SPSS statistics for Windows, version 22 Armonk, NY: IBM Corp.

Diffusion MRI.

A students *t*-test was used to evaluate the differences in MD, FA, AD and RD values between groups. We tested one-sided since we expect the MD, AD and RD values to be higher and the FA values to be lower in ALS cases. Between the groups, there was a significant difference in fixation time (*p=0.003*). Since it is known that fixation time can cause a reduction in FA, MD and AD and an increase in RD (D'Arceuil & de Crespigny, 2007; Schmierer et al., 2008, 2007; Sun, Liang, Xie, Oyoyo & Lee, 2009) a chronic demyelinating disease. Conventional T2-weighted MRI (cMRI, a normalization step was performed before calculating the t-statistics. The normalisation was done by dividing the found FA, MD, AD and RD values in the perforant path by a reference values for each of these metrics in a control region within the same sample. The entorhinal cortex was used as a control region.

Polarized light imaging

A students T-test was used to evaluate the differences in retardance values within the perforant path between ALS cases and controls. We tested one-sided because we expected the retardance values to be lower in ALS cases compared to controls.

The relationship between the retardance and the normalised dMRI diffusion tensor metrics was assessed by calculating the Pearson correlation coefficient. The correlation was tested one sided, because we expected a negative correlation between the MD and retardance and a positive correlation between the FA and the retardance.

Histology

A students T-test was used to evaluate the differences in PLP, SMI-312, CD68 and pTDP-43 stained area fractions. Tissue fixation is known to reduce the availability of antigen binding sites and can therefore cause a decrease in the amount of staining (Werner, Chott, Fabiano & Battifora, 2000). Therefore, a normalisation was performed before calculating the T-test statistics. This normalization was only performed for the PLP and SMI-312 stain. The CD68 and TDP-43 stain were not normalised because inflammation and pTDP-43 pathology are expected to be widespread within the slice even if white matter degeneration is localised.

The normalisation was accomplished by dividing the stained area fraction in the perforant path by the stained area fraction in a control region within the same specimen. The EC was used as a control region. A Pearson correlation analysis was performed on the normalised dMRI and histology values.

Results

Magnetic Resonance Imaging

We aimed to identify the perforant path in all specimens using probabilistic tractography. After

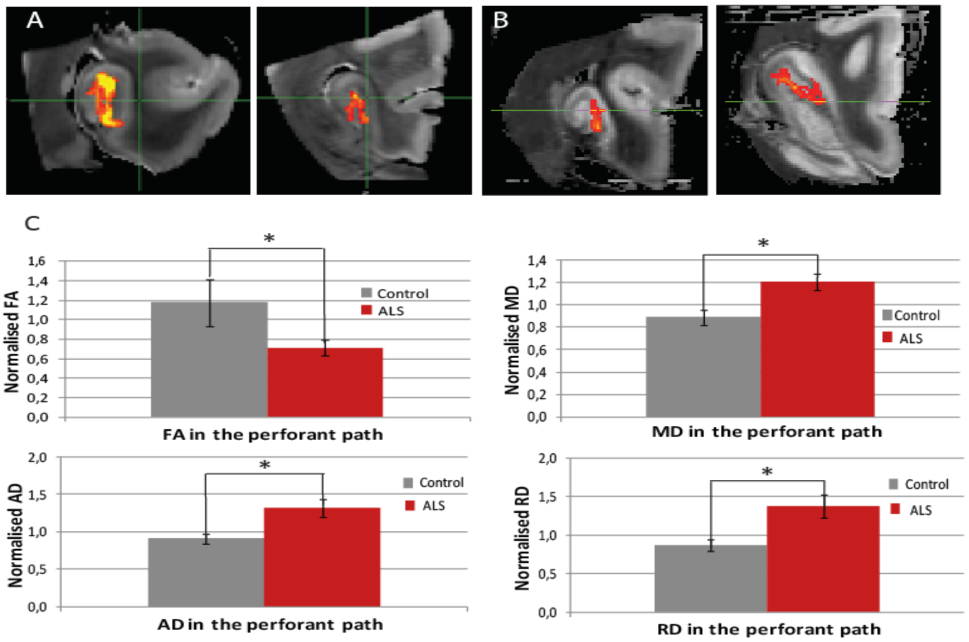

Figure 8. Examples of the tracts representing the perforant pathway running from the subiculum to the dentate gyrus for controls (A) and (B) for ALS cases. These tracts were used for computing the MD, RD, AD and FA values within the perforant path. (C) The FA value in the part of the perforant path that runs from the subiculum to the dentate gyrus is lower in ALS cases compared to controls (p = 0.014, T-test, one-sided). The MD value is significantly higher in the perforant path in the ALS specimen compared to controls (p = 0.011, T-test, one-sided) as well as the AD (p = 0.023, T-test, one-sided) and the RD (p = 0.028, T-test, one-sided) value.

running tractography analysis the identified tracts were inspected and exclusion masks were drawn in such a way that only the tracts representing the anatomical course of the perforant path were maintained for analysis (Fig. 8A).

To get an impression of white matter degeneration in the perforant path, the diffusion tensor metrics were compared between ALS cases and controls. Within the perforant path the FA values were significantly lower in ALS specimens compared to controls (p = 0.014), T-test one-sided). A reduced FA indicates that water diffuses more isotropically and could indicate myelin degeneration. This hypothesis is further strengthened by the increase that was found in MD in ALS specimens compared to controls (p = 0.011, T-test one-sided) (Fig. 8B and C). In addition, both RD (p = 0.028) and AD (p = 0.023) values were significantly higher in ALS cases compared to controls. An increase in RD value is caused by an increasing amount of diffusion along the radial diffusion direction, further implying loss of fibres.

Polarized light imaging

To get a detailed insight in the directionality and myelination of fibres within the tissue, PLI was performed. From the raw PLI data, the fibre orientation, transmittance, retardance and in-plane map were extracted. The transmittance map reflects the amount of light passing through the tissue. Grey matter lets through more light than white matter and therefore appears brighter in the transmittance map (Fig. 9A). The retardance map shows the degree to which the phase of the light is shifted due to interaction with the myelin and is therefore an indirect measure of myelin (Fig. 9B). The in-plane map gives the in-plane direction of the fibres with values ranging from 0 to π (Fig. 9C). The fibre orientation map is formed by combining the retardance and in-plane maps. It shows the direction of the myelinated fibres within the tissue, allowing for tracing the perforant path within each slice (Fig. 9D).

Retardance

To further investigate the amount of white matter in the perforant path in ALS, patients compared to controls and the PLI retardance maps were analysed. As previously mentioned, retardance measures how much a polarized light wave is shifted due to interaction with regularly arranged myelin sheets. The PLI retardance values within the perforant path were calculated and it was shown that the retardance values in ALS cases were lower, implicating a loss of myelin. However, the decrease was not significant (p

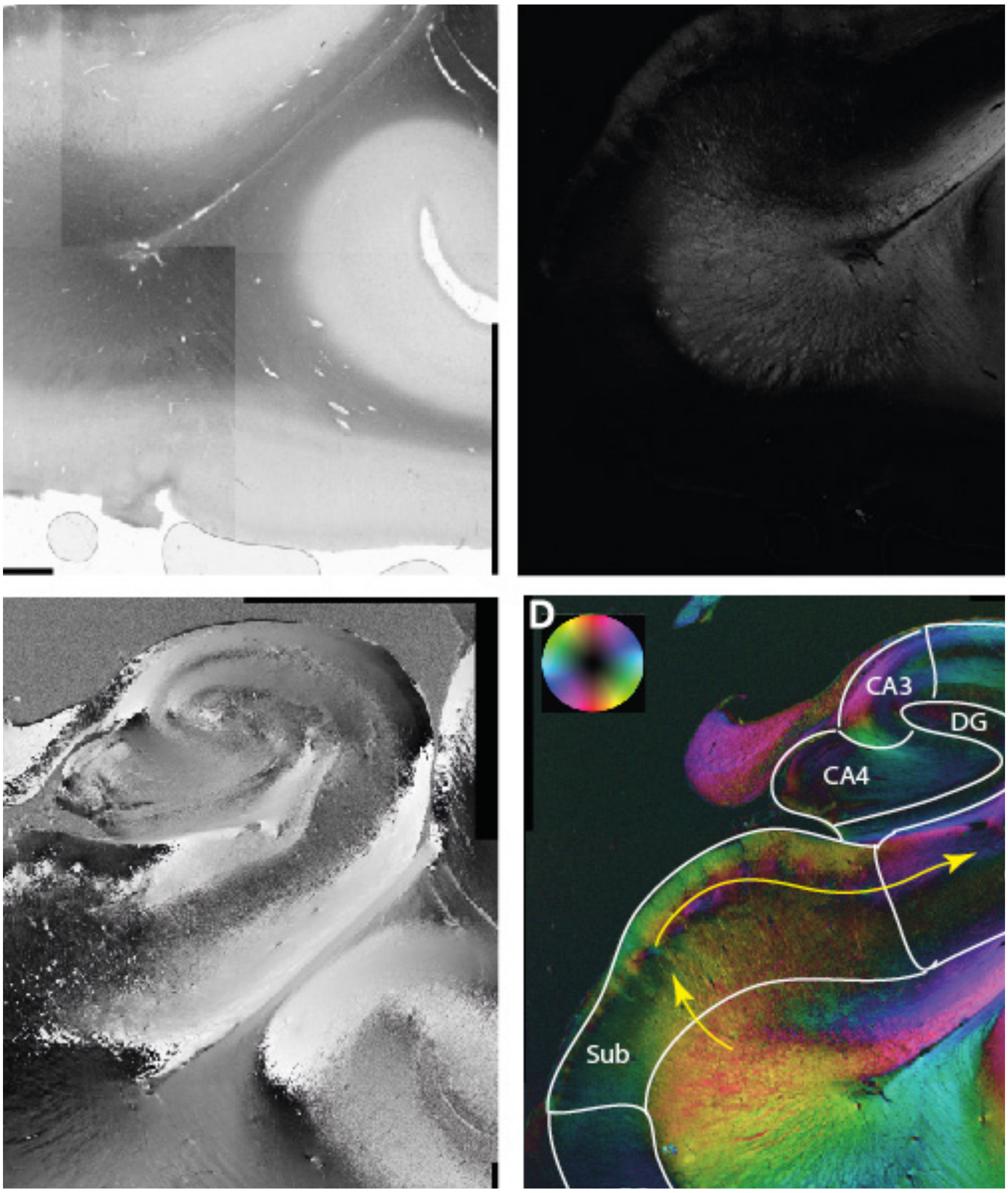

Figure 9. Example of the polarised light imaging data from a control case. (A) The transmittance map reflecting the amount of light passing through the tissue. (B) The retardance map showing the degree to which the light is shifted due to interaction with the myelin. (C) The in-plane map giving the in-plane direction of the fibres with values ranging from 0 to π. (D) The fibre orientation map showing the directionality of the myelinated fibres indicated with the colour wheel. This map is formed by combining the retardance and in-plane map. The anatomical regions within the hippocampus are delineated and the approximate direction of the perforant path is indicated with the yellow arrows.

= 0.16, one-sided; Fig. 10A).

Since PLI is a relatively new technique and to our knowledge not applied to pathological specimens before, we aimed to gain insight in the relationship between the dMRI metrics and the PLI retardance values. The PLI values were therefore correlated with the FA and MD. As expected, there was a positive correlation between the retardance and the FA ($p = 0.038$, one-sided). No correlation was found between the retardance and the MD ($p = 0.48$, one-sided; Fig. 10C). We, however, expected a negative correlation between the MD and retardance because an increase in MD is thought to reflect a decrease in white matter structure.

Dispersion

As a result of fibre degeneration, orientation dispersion may be a marker for the disturbed coherence of fibres. Indeed, the fibre dispersion was elevated in ALS cases compared to controls ($p = 0.044$), demonstrating an increase in the fanning of fibres within the perforant path (Fig. 11C). These results further implicate damage of the perforant path.

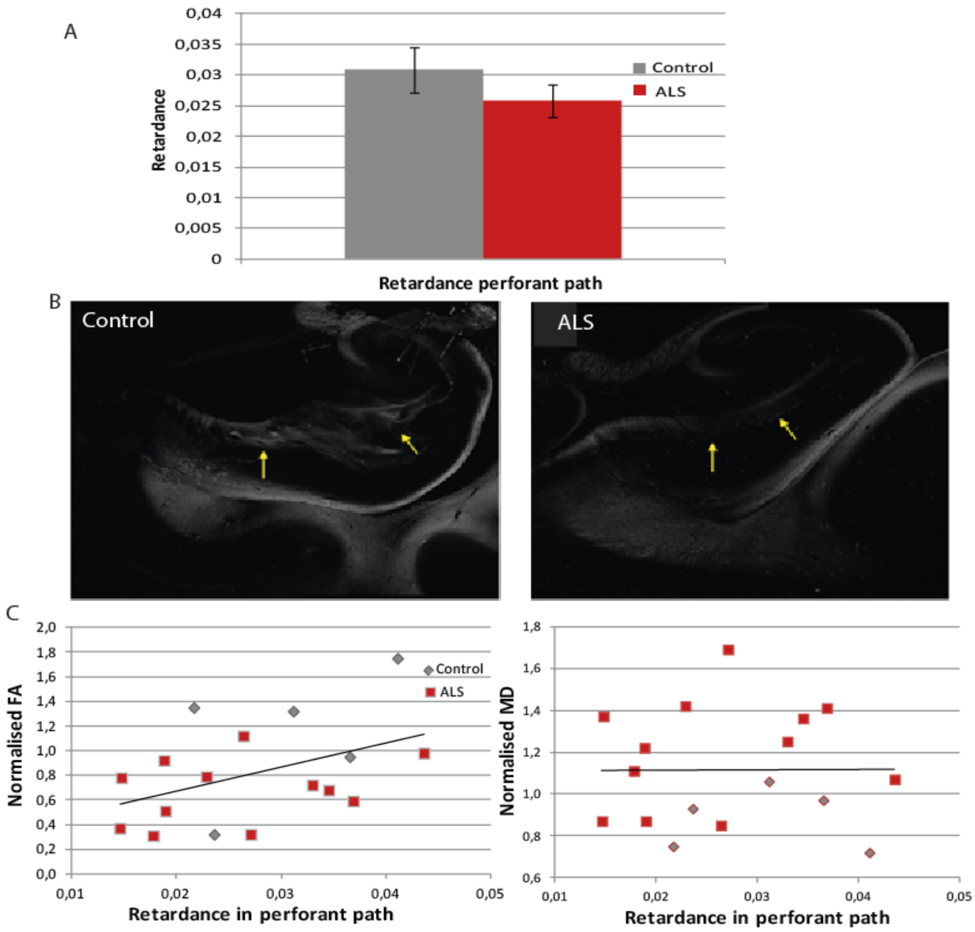

Figure 10. (A) The retardance value within the perforant path was found to be lower in ALS cases compared to controls, but was not significant ($p = 0.16$ one-sided). (B) Two examples of retardance maps from an ALS case (left) and control (right). The yellow arrows indicate the approximate location of the perforant path. (C) Correlation between the MD and FA values from the dMRI and retardance values from PLI for cases and controls combined. There was a significant correlation between the FA and the retardance ($p = 0.038$ one-sided), but not between the MD and the retardance ($p = 0.48$, one-sided).

Immunohistochemistry

While dMRI and PLI provide valuable information regarding white matter architecture in our specimens, protein pathological information within the tissue is lacking from these techniques. To gain more insight in the protein pathology, we performed immunohistochemical stains for pTDP-43, microglial activation (CD68), myelin (PLP) and neurofilaments (SMI-312).

The stained area fraction was calculated using an automatic segmentation for all stains. An example of each of these segmentations is shown in Figure 12. The segmentation for PLP and CD68 performed well, meaning that it picked up the true DAB-staining without including the background signal. For SMI-312, the segmentation proved to be more challenging due to a relatively low contrast between the background and true stain. To make sure it would not pick up any background signal, the segmentation settings were set to be more conservative. For this reason, the algorithm sometimes missed out on some of the true staining. To develop an automatic segmentation that correctly identified the pTDP-43 inclusions, it was necessary to set a minimum cluster size threshold of 15 pixels. After setting the size threshold, the amount of pTDP-43 inclusions was in general correctly quantified. However, the algorithm still picked up some degree of non-specific staining of pigments within the nucleus as can be observed in supplementary Figure 3, resulting in some false positive signal.

After determining the segmentation settings, the stained area fraction was computed for each stain in both cases and controls. A higher amount of myelin (PLP) was found in ALS cases compared to controls. However, this difference was not significant ($p = 0.11$). Furthermore, an increase in the amount of neurofilaments (SMI-312) was detected in ALS cases

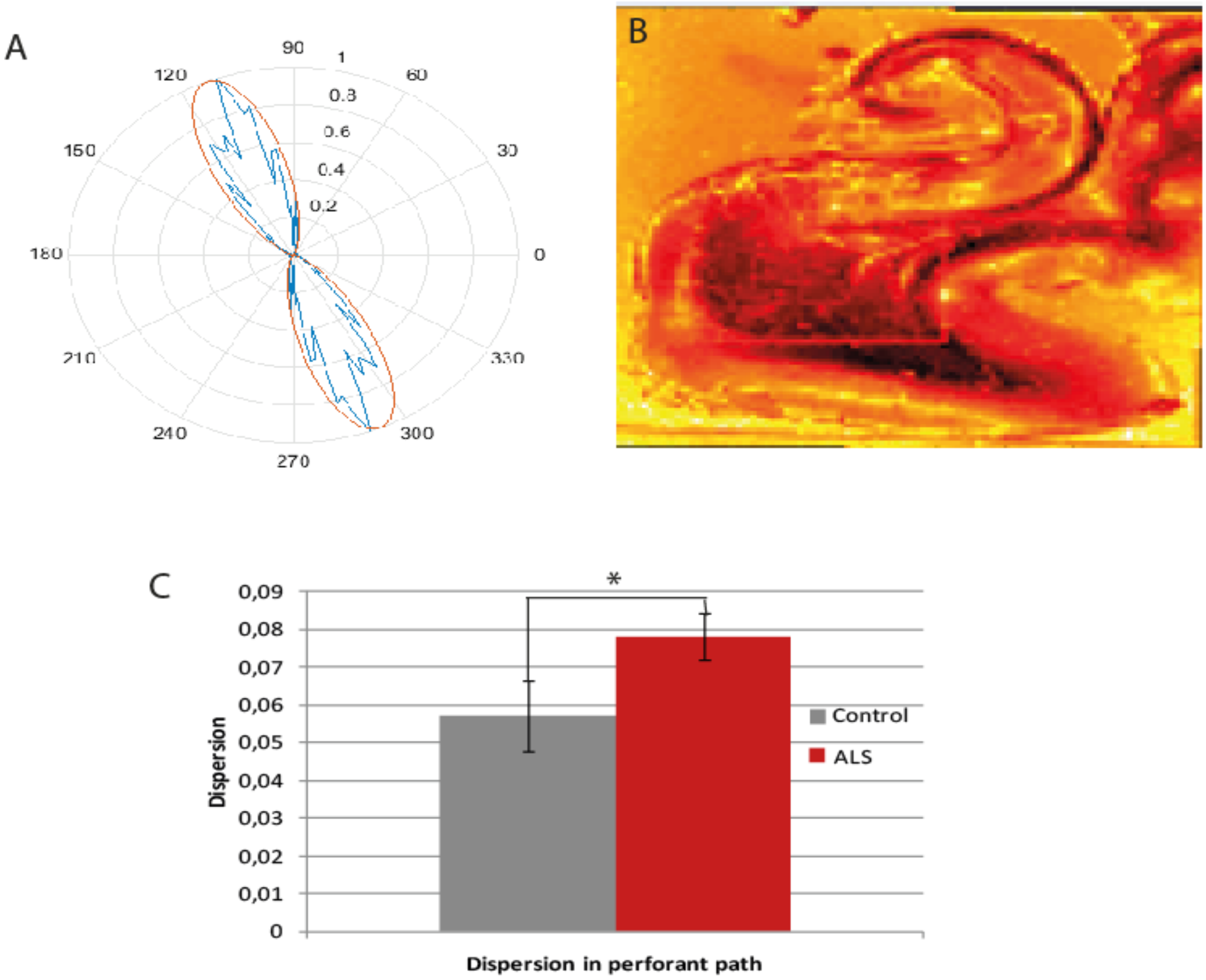

Figure 11. (A) A polar plot illustrating the raw PLI fibre orientation distribution (blue) from an exemplar neighbourhood of 50x50 pixels fitted with a von Mises distribution (red). (B) An example of the log(1/κ)-map. K is a measure for the broadness of the Von-Mises distribution, the higher the K value, the narrower the Von-Mises distribution. A narrow Von Mises distribution is associated with a low level of dispersion. Therefore, 1/κ is a measure for the amount of dispersion. Log (1/κ) was shown to increase visibility of the dispersion values. It can be observed that dispersion is lower in highly aligned white matter regions. (C) The amount of dispersion is higher in ALS cases compared to controls within the perforant path ($p = 0.044$).

($p = 0.03$). These results contradict our previous findings with dMRI and PLI since they suggested a decrease in myelination and axonal integrity in ALS cases compared to controls. No changes were observed in the amount of CD68, indicating similar levels of inflammation in both groups. Finally, it was shown that two out of the 13 ALS cases exhibited pTDP-43 pathology within the hippocampus (Fig. 13B).

To investigate the relationships between PLI and SMI312 staining and the dMRI metrics, correlation analyses were performed. As expected, a positive correlation was present between the amount of myelin and the amount of neurofilaments ($p = 0.025$, $R^2 = 0.499$). An increase in MD and RD has previously been associated with demyelination. A negative correlation was therefore expected between PLP and MD/RD. However, contradictory to our hypothesis, a positive correlation was found between PLP and MD ($p = 0.037$, $R^2 = 0.458$), PLP and RD ($p = 0.023$, $R^2 = 0.506$) and PLP and AD ($p = 0.021$, $R^2 = 0.514$). The amount of SMI-312 stain did not correlate with any of the diffusion measures.

Discussion

Since ALS is mostly known as a motor disease, multiple studies investigating white matter alterations in ALS have focused on changes in the cortico-spinal tract and the corpus callosum (Cirillo et al., 2012; Filippini et al., 2010; Horsfield & Jones, 2002; Lillo et al., 2012). The clinical involvement of both compartments is characteristically variable and the site of onset debated. We sought to establish

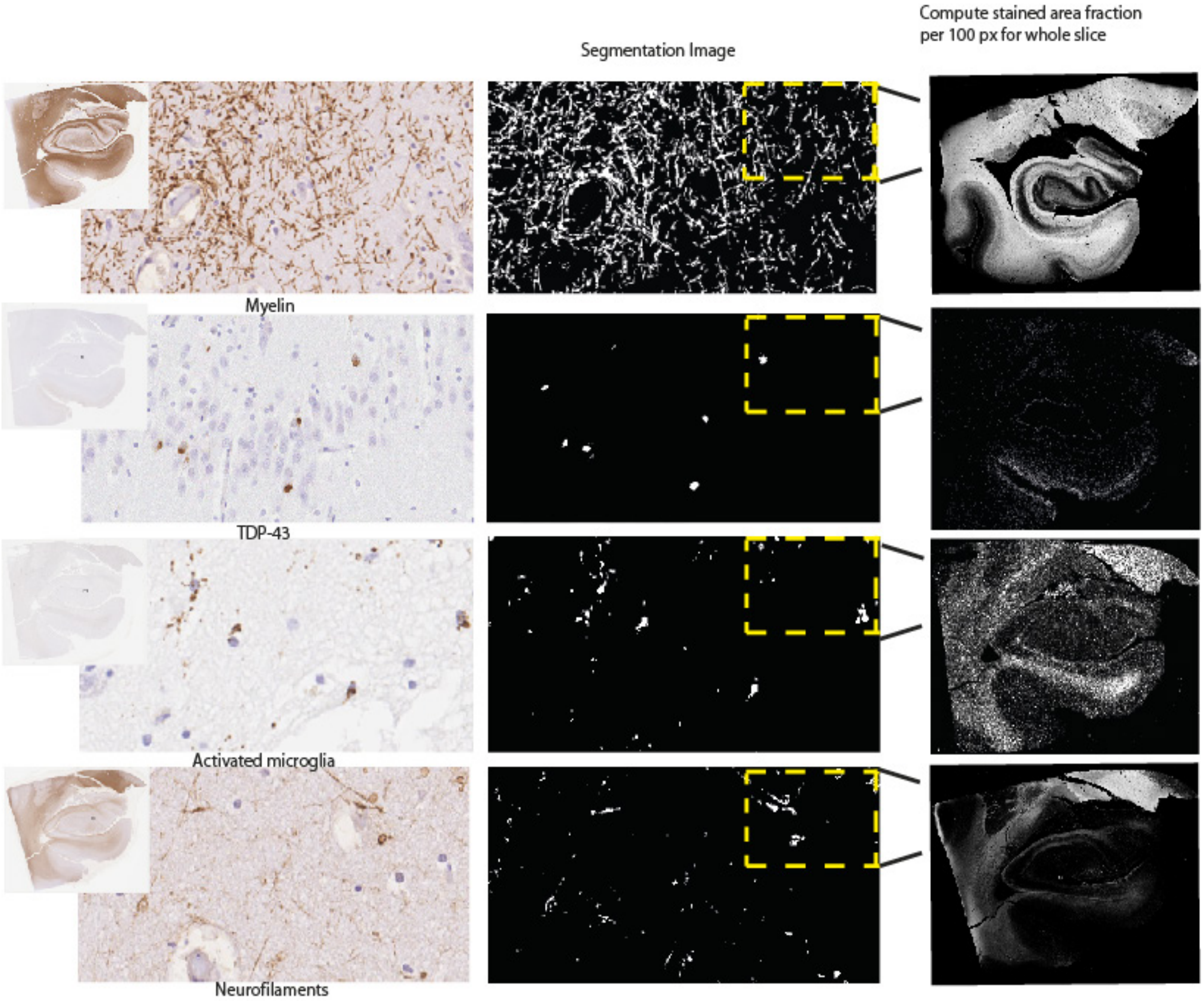

Figure 12. Overview of the histological data and analysis. The left column shows a snapshot of the original staining for myelin, TDP-43, activated microglia and neurofilaments. The middle column depicts the automatic segmentation of this snapshot where white indicates a pixel that is considered to be stained and black indicates a pixel that is considered to be background. After segmentation, the stained area fraction was calculated per 100 pixels resulting in a down-sampled image reflecting the amount of staining over the slice (yellow square). The right column gives an overview of the segmentation across the entire slice.

whether there is a consistent signature of cerebral white matter abnormalities in heterogeneous ALS cases. In this observational study, diffusion tensor imaging was applied in a whole-brain analysis of 24 heterogeneous patients with ALS and well-matched healthy controls. Tract-based spatial statistics were used, with optimized voxel-based morphometry of T1 images to determine any associated gray matter involvement. A consistent reduction in fractional anisotropy was demonstrated in the corpus callosum of the ALS group, extending rostrally and bilaterally to the region of the primary motor cortices, independent of the degree of clinical upper motor neuron involvement. Matched regional radial diffusivity increase supported the concept of anterograde degeneration of callosal fibers observed pathologically. Gray matter reductions were observed bilaterally in primary motor and supplementary motor regions, and also in the anterior cingulate and temporal lobe regions. A post hoc group comparison model incorporating significant values for fractional anisotropy, radial diffusivity, and gray matter was 92% sensitive, 88% specific, with an accuracy of 90%. Conclusion: Callosal involvement is a consistent feature of ALS, independent of clinical upper motor neuron involvement, and may reflect independent bilateral cortical involvement or interhemispheric spread of pathology. The predominantly rostral corticospinal tract involvement further supports the concept of independent cortical degeneration even in those patients with ALS with predominantly lower motor neuron involvement clinically. Over the past years, ALS has become more and more recognized as a multisystem neurodegenerative disease because areas of the brain outside the motor-areas also undergo

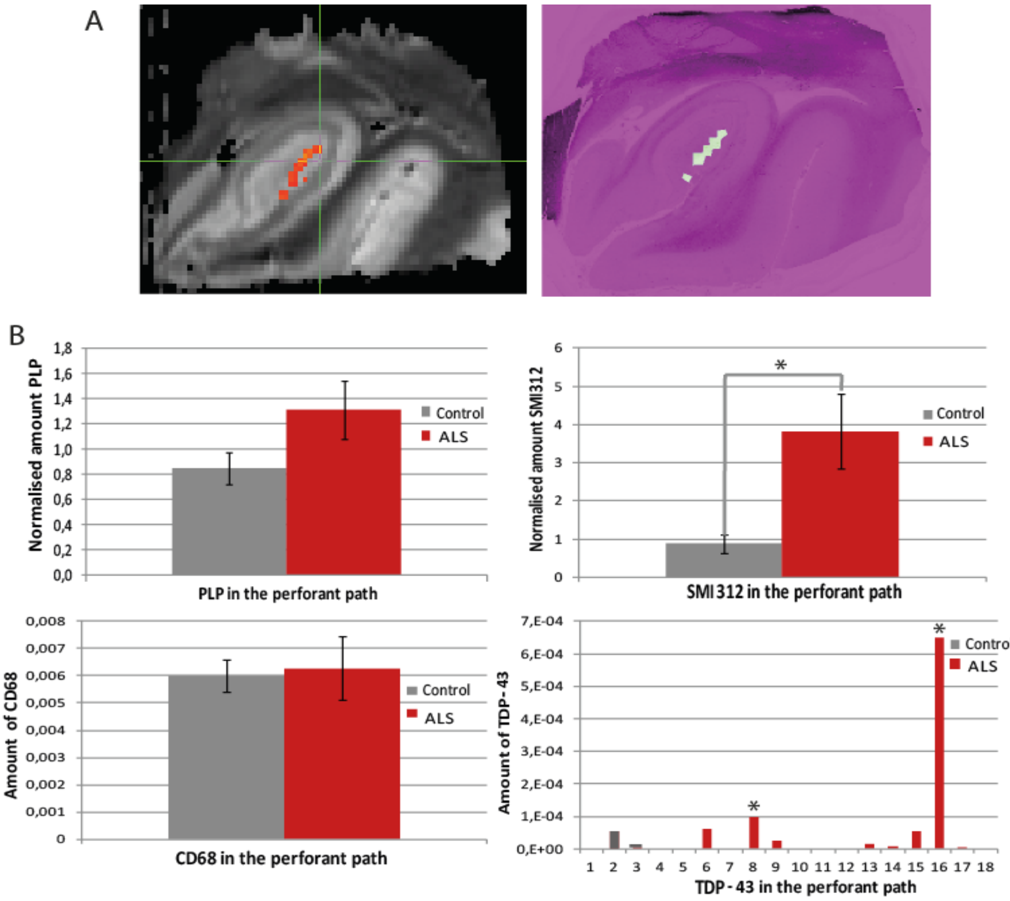

Figure 13. (A) Example of manual delineation of the perforant path (right) based on the dMRI tractography results (left). (B) The amount of PLP within the perforant path is higher in ALS cases compared to controls, but not significantly (*p*=0.11). Furthermore, an increase in the amount of neurofilaments is observed in ALS cases (*p* = 0.03). The amount of inflammation (CD68) is similar in both groups and two out of the 18 cases exhibit pTDP-43 pathology within the perforant path.

degeneration. Furthermore, around 50% of the ALS patients exhibit cognitive problems with 10-20% of the people meeting the criteria for bvFTD. Despite the relationship between ALS and memory deficits, detailed investigation of white matter tracts related to memory has been lacking to date. Here, we used dMRI, PLI and histology to investigate white matter changes in the perforant path, a projection of the circuit of Papez that has been implicated to be affected in ALS and bvFTD and was previously linked to cognitive deficits in Alzheimer's disease (Hyman et al., 1986; Thal et al., 2000).

Using dMRI, we demonstrated a reduction in the FA and an increase in the MD, AD and RD in the perforant path in ALS cases compared to controls (Fig. 8B and C), suggesting white matter damage. PLI retardance values were also lower in ALS specimens, however, a significant difference was not detected (Fig. 10A). The retardance did correlate with the FA, but not with the value MD within the perforant path (Fig. 10C). The amount of dispersion was significantly higher in ALS specimens, further indicating damaged axonal structure (Fig. 11C). Histochemical analysis showed no differences in the amount of microglial activation. However, they did show a (non-significant) increase in myelin and a significant increase in the amount of neurofilaments. There was a positive correlation between PLP and MD and RD and AD dMRI values. pTDP-43 pathology was found in two out of the 14 ALS cases within the hippocampus (Fig. 13B).

In order to extract the FA, MD, AD and RD values from dMRI within the perforant path, probabilistic tractography was performed. At first, tractography was performed by using the EC as a seed, keeping all paths terminating in the DG. With these settings we were unable to track the perforant pathway. Next, we tried to extract the perforant path by using the EC as a seed and the Sub as waypoint, again only maintaining the paths terminating at the DG. With these settings, it was also not possible to extract a path representing the anatomical course of the perforant path (Supplementary Fig. 1). This is in concordance with Augustinack and colleagues (2010), who also reported to be unable to track the whole perforant pathway from the EC to DG using tractography.

Third, we decided to divide the perforant path into two parts: One part from the EC to the Sub and the other part from the Sub to the DG. However, in the area from the EC to the Sub, two other fibre bundles, the alvear path and the collateral white matter, are crossing the perforant path (Supplementary Fig. 5). This makes it difficult to solely extract the perforant path for analysis in this region. Furthermore, the perforant path is originating from across the entire entorhinal cortex forming a coherent bundle only from the subiculum on. Since we are only interested in the dMRI, PLI and histology metrics within the perforant path, we decided to solely focus on the part of the path running from the Sub to the DG.

Part of the changes that were found in the dMRI metrics in ALS patients compared to controls have been linked to a loss of white matter integrity. Namely, a reduction in FA and an increased MD and RD values were repeatedly associated with white matter degeneration (Bozzali et al., 2002; Soares, Marques, Alves & Sousa, 2013). Interpretation of the increase in AD is less arbitrary as some studies found no changes in AD due to demyelination (Klawiter et al., 2011; Song et al., 2002), while other studies either find an increase in AD (Metwalli et al., 2010) or a decrease in AD due to white matter loss (Harsan et al., 2006; Tyszka et al., 2006). Possibly, an increase in AD is observed due to enlargement of the extracellular space as a result of axonal degeneration.

While the dMRI results suggest that white matter in the perforant path is damaged in ALS cases, changes in the dMRI metrics can also be driven by several other factors. Since dMRI metrics are calculated based on the diffusion of water, assuming that water diffuses along the line of an axon, they are indirect measures of the white matter geometry. For example, two kissing or crossing fibres could yield an FA value of 0 implying fully isotropic diffusion and no axons being present, not reflecting the actual white matter structure within that voxel (Jbabdi & Johansen-Berg, 2011). However, large differences between cases and controls in the amount of crossing fibres are not expected since we are investigating the same pathway in a similar area in both groups

Besides a change in white matter geometry, the diffusion metrics can also be affected by the way tissue is preserved after death. Several of the ALS cases had post–mortem intervals (PMI) of up to five days. Previous research has shown that long PMI can cause a reduction in FA and an increase in MD values (D'Arceuil & de Crespigny, 2007; Miller et al., 2011) and as a link between in vivo diffusion studies and \"gold standard\" histology/dissection. While there is a relatively mature literature on post mortem diffusion imaging of animals, human brains have proven more challenging due to their incompatibility with high-performance scanners. This study presents a method for post mortem diffusion imaging of whole, human brains using a clinical 3-Tesla scanner with a 3D segmented EPI spin-echo sequence. Results in eleven brains at 0.94. 0.94. 0.94. mm resolution are presented, and in a single brain at 0.73. 0.73. 0.73. mm resolution. Region-of-interest analysis of diffusion tensor parameters indicate that these properties are altered compared to in vivo (reduced diffusivity and anisotropy) but there are relatively few studies in human brains. While animal tissues are generally fixed pre-mortem or directly post-mortem, this is not possible for human tissue, therefore there is always some delay between death and tissue fixation. The elapsed time between death and tissue fixation, the post-mortem interval (PMI). In our data, a significant negative correlation between the PMI and the MD values (p = 0.009) was observed. No significant correlation was found between the FA (p = 0.242) or retardance (p = 0.647) and the PMI. Another factor that can influence the dMRI values is the fixation time. It has previously been shown that fixation causes a reduction in diffusivity within the tissue, leading to a drop in FA, MD, AD and RD (D'Arceuil & de Crespigny, 2007; Sun et al., 2009, 2005) but relatively few studies in human brains. While animal tissues are generally fixed pre-mortem or directly post-mortem, this is not possible for human tissue, therefore there is always some delay between death and tissue fixation. The elapsed time between death and tissue fixation, the post-mortem interval (PMI. Because the fixation time between groups differs significantly (p = 0.003), it is important to correct for these effects. Based on the assumption that any effects of PMI and fixation time are present in the whole hippocampal tissue block, an internal control region was used to normalise the FA, MD, AD and RD values within the perforant path.

First, the collateral white matter was chosen as a control region as this white matter region was present in all sampled hippocampal blocks. However, an (non-significant) increase in the MD value was observed within the collateral white matter (p = 0.15), while the expected effect of fixation time was in the opposite direction. In addition, the perforant path was partially crossing through the collateral white matter area (Supplementary Fig. 5), making the collateral white matter an unsuitable control region. Unfortunately, there was no other white matter region that was present in all sampled hippocampal blocks and that was not part of the circuit of Papez. Therefore, the EC was used as a control region. The perforant path originates here but very few fibres of perforant path run through this area. After normalisation, a significant decrease in the FA value ($p = 0.014$) and a significant increase in the MD value ($p = 0.011$), AD value ($p = 0.021$) and RD value ($p = 0.028$) was found in ALS cases compared to controls (Fig. 8C). For future research, specimens have to be matched on fixation time, PMI, age, gender and region to ensure that any observed differences are driven by case-control differences.

The dMRI results implicate white matter loss in the perforant path in ALS but can, as previously mentioned, also be caused by a difference in fibre configuration between the groups. We performed PLI and histology to gain further insight in the nature of the changes found with dMRI.

The PLI retardance maps were used to compare the degree of myelination between patients and controls. This is, to our knowledge, the first time that PLI was used to make a case-control comparison. A decrease in the retardance was observed in ALS cases compared to controls within the perforant path. This decrease was, however, not significant ($p = 0.16$, one-sided, Fig. 10A).

In addition to the birefringent properties of myelinated axons, the retardance is also dependent on the inclination angle of fibres. A reduction in retardance is for example observed when equally myelinated fibres are propagating less radial to the imaging plane (Axer et al., 2011)the structural basis of the human connectome. In contrast to animal brains, where a multitude of tract tracing methods can be used, magnetic resonance (MR). A small tilt in the plane could have been induced during cutting the sections or during sampling of the hippocampal blocks from the brains, leading to a variation in the retardance values.

We were unable to perform a fixation time correction on the retardance values because the exact effects of fixation time on retardance are unknown. Retardance measures the birefringence induced by the regular arrangement of myelin proteins and lipids. During formalin fixation, proteins are cross-linked keeping protein structures relatively intact (Thavarajah, Mudumbaimannar, Rao, Ranganathan & Elizabeth, 2012). It has been shown that there is a loss of lipids in the central nervous system during fixation, possibly resulting in lower retardance values when fixation time is increasing (Hopwood, 1969). However, no significant negative correlation between fixation time and retardance values was found ($R^2 = 0.306$, $p = 0.109$, one-sided). Another inadequacy is that the effect of aggregations of proteins like pTDP-43 on the retardance signal have never been investigated.

To gain further insight in the relationship between retardance and dMRI metrics, a Pearson correlation analyses was performed. There was a positive correlation between the FA and retardance, meaning that a higher retardance value was associated with a more isotropic water diffusion direction and supposedly a more intact white matter architecture. Surprisingly, no negative correlation between the MD and retardance was observed. It was expected that when the MD value rises due to loss of axonal integrity, the retardance values would go down. Potentially, the decrease in MD value is more a result of loss of coherence in fibre structure than of demyelination and severe degeneration of axons.

To further investigate the degree of myelination within the perforant path, immunohistochemical stainings for proteolipid protein (PLP) were performed. Myelin consists of a high proportion of lipids (75-80%) and consequently a lower portion of proteins (15-30%). PLP and myelin basis protein (MBP) together make up about 60-80% of the proteins present in myelin (Brady & Siegel, 2012). Since PLP is one of the main components of myelin, a reduction in PLP is expected when myelin is degrading (Garbern et al., 2002). Instead, our results indicate a (non-significant) increase in PLP in the subiculum in ALS cases compared to controls ($p = 0.11$, one-sided). This result is contradicting the previously discussed dMRI and PLI results suggesting a reduction in white matter. Possibly, the change in white matter structure is driven by a reduction in MBP or lipids, unrelated to the amount of PLP. Another reason for the discrepancy between the dMRI and PLI and the PLP stain could be that axonal degeneration is occurring in the absence of demyelination (Garbern et al., 2002). As a result, axons would proceed to disentangle, increasing the amount of myelin-stained surface. The spreading of axonal fibres is known to be the begin stage of Wallarian degeneration (Waller, 1850). The significant increase in the spreading of fibres (dispersion, $p = 0.044$) and the positive correlation between the MD, RD and AD values and the PLP stain further substantiates this hypothesis.

An increase in the amount of SMI-312 stain was observed, again contradicting our hypothesis and the dMRI and PLI results. However, several previous papers report that during axonal degeneration in ALS swollen axon segments occur that are rich of the neurofilament proteins that SMI-312 stains for (Delisle & Carpenter, 1984; Lingor et al.,

2012) inflammatory and degenerative neurological diseases. Increasing evidence suggests that axonal degeneration occurs early in the course of these diseases and therefore represents a promising target for future therapeutic strategies. We review the evidence for axonal destruction from pathological findings and animal models with particular emphasis on neurodegenerative and neurotraumatic disorders. We discuss the basic morphological and temporal modalities of axonal degeneration (acute, chronic and focal axonal degeneration and Wallerian degeneration. The increase in SMI-312 stain could thus be caused by accumulation of neurofilaments in these axonal swellings. Another possible rationale behind the increase in neurofilaments is that accumulation of phosphorylated neurofilaments is often observed in the amyloid beta plaques associated with aging and Alzheimer's disease (Dale & Garcia, 2012; Dickson, King, McCormack & Vickers, 1999). The degree of amyloid beta like pathology should be taken into account as soon as the diagnostic stains are fully evaluated.

pTDP-43 pathology was detected in only two out of the 13 ALS cases within the hippocampal area. In one case, mild pathology was observed; in the other case, the pathology was classified as frequent (Fig. 3). Tan and colleagues (2015) developed a staging system for pTDP-43 pathology in ALS and FTD and it is shown that the hippocampal area is one of the last areas to be affected by pTDP-43 pathology in ALS. It is thus not surprising that not all specimens exhibit hippocampal pathology. In bvFTD however, the hippocampus is one of the first areas to be enforced by pTDP-43.

The histology data showed no differences in the amount of activated microglia, a measure for inflammation, in ALS cases compared to controls. This contradicts earlier findings of enhanced microglial activation in white matter lesions in ALS in the corpus callosum and the spinal cord (Henkel et al., 2004; Sugiyama et al., 2013). However, the average age of the control specimens was 70.8 years. It is known that the amount of activated microglia increases upon aging, potentially making it harder to detect significant differences in microglial activation between groups (Sparkman & Johnson, 2008). In our data, we did not find a correlation between activated microglia and age. Until now, only one section per subject was stained and analysed. Increasing sample size could result in a significant difference in CD68 staining between the groups.

The fact that only one section per subject was stained for each histochemical stain also resulted in a regional difference between the control and ALS cases. On average, the control sections were more representative of the posterior part of the hippocampus while the ALS sections represented a more anterior part (supplementary Fig. 3). Unfortunately, these regional differences were not only present in the single histology slices but also in the sampled hippocampal blocks. The control blocks were sampled in Nijmegen, The Netherlands, while the ALS blocks were sampled in Oxford, United Kingdom. Despite the fact that both groups used the LGN as an anatomical reference point for sampling the blocks, the control blocks were sampled more posterior than the ALS blocks. It could thus be that the observed dMRI, PLI and histology differences were driven by regional differences rather than by case-control variation. It is, however, hard to correct for this.

To allow further research of white matter changes in the entire circuit of Papez, other regions of the circuit were also sampled from all specimens. Unfortunately, we were not able to use ALS/FTD or pure bvFTD specimens for this research. It would be interesting to see whether the observed white matter changes correlate with clinically observed cognitive decline. Since the magnitude of all dMRI metrics is going down as a result of fixation, it is also interesting to perform *in vivo* dMRI of the perforant path in controls, ALS/ALS-FTD and bvFTD patients. This is challenging because the perforant path is small and therefore hard to detect with tractography analysis. Because we used post-mortem tissue, we were able to work with long scanning times (3-4 hours) and an ultra-high field MRI scanner (11.7T) resulting in very high resolution dMRI. Routine clinical MRI scanners have a field strength of 1.5-3T and scanning time would be maximally an hour, drastically reducing the achievable resolution. Another interesting target of future research is the effect of fixation time and protein aggregation on retardance measures. Since PLI is a new technique, this remains largely unknown so far.

Our current results linked the perforant path, a memory related white matter tract, to ALS. This research therefore contributes to the hypothesis of ALS being a multisystem neurodegenerative disease. Till now, the main focus in ALS research has been on motor neuron degeneration and degeneration of motor related areas and pathways. Instead, our research has focussed on a potential neural substrate of the cognitive problems that are observed in 50% of the ALS patients. We aimed to shed more light on the cause of these memory related problems and thereby hope to raise awareness about this under exposed aspect of the disease. Hopefully, our results will contribute to faster recognition and alleviation of cognitive disabilities in ALS patients in the clinic.

Furthermore, our research substantiates the hypothesis that ALS and bvFTD are a spectrum of diseases rather than two separate disorders, by linking a pathway that is known to be involved in bvFTD to ALS. Future studies should therefore focus on investigating the perforant path in bvFTD and ALS/bvFTD patients to see if damage to the perforant path directly correlates with the degree of cognitive deficits in these diseases.

Conclusion

This work investigated white matter changes in the perforant path in ALS patients using dMRI, PLI and histological analyses. A reduction in the FA and an increase in the MD, AD and RD observed in ALS cases relative to controls, implicating white matter degeneration of the perforant path. This observation was supported by a (non-significant) decrease in the PLI retardance values and increased dispersion in the perforant path. However, histology results showed an increase in PLP and neurofilaments, potentially due to disentangling of axonal fibres and neurofilamental aggregation in axonal swellings, respectively.

We conclude that the axonal integrity of the perforant path is damaged in ALS cases compared to controls. Our worked hereby provides further proof of ALS being a multisystem disease and therefore contributes to the understanding of ALS. Since the perforant path is also implicated in bvFTD, we provide further evidence of ALS and bvFTD being a spectrum of diseases. Furthermore, we show that white matter degeneration of the perforant path likely occurs even before clinical diagnosis of cognitive symptoms. Finally, our results provide the perforant path as a potential neural correlate of the cognitive symptoms in ALS and further research should be done to substantiate this hypothesis.

Acknowledgements

We would like to acknowledge “Stichting Alzheimer Nederland” for their funding support. Furthermore, we would like to acknowledge P.J.W.C. Dederen for instructing in the cutting of the sections for PLI. Furthermore, we’d like to thank Dr. M. Wiessman for his excellent support with the MRI protocols and C. Grabitz and J. de Ruyter van Steveninck for their lab work. Finally, we acknowledge the Oxford brain bank as well as the body Donor program from the department of Anatomy, Radboud UMC Nijmegen for providing the post-mortem specimens.

References

Augustinack, J.C., Helmer, K., Huber, K.E., Kakunoori, S., Zöllei, L., & Fischl, B. (2010). Direct visualization of the perforant pathway in the human brain with ex vivo diffusion tensor imaging. *Frontiers in Human Neuroscience. 4*, 42.

Aung, W.Y., Mar, S., & Benzinger, T.L. (2013). Diffusion tensor MRI as a biomarker in axonal and myelin damage. *Imaging Med.*

Axer, M., Amunts, K., Grässel, D., Palm, C., Dammers, J., Axer, H., Pietrzyk, U., & Zilles, K. (2011). A novel approach to the human connectome: Ultra-high resolution mapping of fiber tracts in the brain. *Neuroimage. 54*, 1091–1101.

Barbagallo, G., Nicoletti, G., Cherubini, A., Trotta, M., Tallarico, T., Chiriaco, C., Nisticò, R., Salvino, D., Bono, F., Valentino, P., & Quattrone, A. (2014). Diffusion tensor MRI changes in gray structures of the frontal-subcortical circuits in amyotrophic lateral sclerosis. *Neurological Science. 35*, 911–918.

Bastiani, M., & Roebroeck, A. (2015). Unraveling the multiscale structural organization and connectivity of the human brain: the role of diffusion MRI. *Frontiers in Neuroanatomy. 9,* 77.

Behrens, T.E.J., Berg, H.J., Jbabdi, S., Rushworth, M.F.S., & Woolrich, M.W. (2007). Probabilistic diffusion tractography with multiple fibre orientations: What can we gain? *Neuroimage 34,* 144–155.

Behrens, T.E.J., Woolrich, M.W., Jenkinson, M., Johansen-Berg, H., Nunes, R.G., Clare, S., Matthews, P.M., Brady, J.M., & Smith, S.M. (2003). Characterization and Propagation of Uncertainty in Diffusion-Weighted MR Imaging. *Magn. Reson. Med. 50*, 1077–1088.

Bonafede, R., & Mariotti, R. (2017). ALS Pathogenesis and Therapeutic Approaches: The Role of Mesenchymal Stem Cells and Extracellular Vesicles. *Frontiersin Cellular Neuroscience. 11.*

Bott, N.T., Radke, A., Stephens, M.L., & Kramer, J.H. (2014). Frontotemporal dementia: diagnosis, deficits and management. *Neurodegener. Dis. Manag. 4,* 439–54.

Bozzali, M., Falini, A., Franceschi, M., Cercignani, M., Zuffi, M., Scotti, G., Comi, G., & Filippi, M. (2002). White matter damage in Alzheimer’s disease assessed in vivo using diffusion tensor magnetic resonance imaging. *J. Neurol. Neurosurg. Psychiatry* 72, 742–746.

Brady, S.T., & Siegel, G.J. (2012). Characteristic composition of myelin. Basic Neurochem. *Princ. Mol. Cell. Med. Neurobiol. 1096.*

Brettschneider, J., Del Tredici, K., Irwin, D.J., Grossman, M., Robinson, J.L., Toledo, J.B., Fang, L., Van Deerlin, V.M., Ludolph, A.C., Lee, V.M.Y., Braak, H., & Trojanowski, J.Q. (2014). Sequential distribution of pTDP-43 pathology in behavioral variant frontotemporal dementia (bvFTD). *Acta Neuropathol. 127*, 423–439.

Brettschneider, J., Del Tredici, K., Toledo, J.B., Robinson, J.L., Irwin, D.J., Grossman, M., Suh, E., Van Deerlin, V.M., Wood, E.M., Baek, Y., Kwong, L., Lee, E.B., Elman, L., McCluskey, L., Fang, L., Feldengut, S., Ludolph, A.C., Lee, V.M.Y., Braak, H. & Trojanowski, J.Q., (2013). Stages of pTDP-43 pathology in amyotrophic lateral sclerosis. *Ann. Neurol. 74,* 20–38.

Cirillo, M., Esposito, F., Tedeschi, G., Caiazzo, G., Sagnelli, A., Piccirillo, G., Conforti, R., Tortora, F., Monsurrò, M.R., Cirillo, S. & Trojsi, F., (2012). Widespread microstructural white matter involvement in amyotrophic lateral sclerosis: A whole-brain DTI study. *Am. J. Neuroradiol. 33,* 1102–1108. 8

Cykowski, M.D., Powell, S.Z., Peterson, L.E., Appel, J.W., Rivera, A.L., Takei, H., Chang, E. & Appel, S.H., (2017). Clinical Significance of TDP-43 Neuropathology in Amyotrophic Lateral Sclerosis. *J. Neuropathol. Exp. Neurol. 76,* 402–413.

D'Arceuil, H. & de Crespigny, A., (2007). The effects of brain tissue decomposition on diffusion tensor imaging and tractography. *Neuroimage, 36*, 64–68.

Dale, J.M., & Garcia, M.L. (2012). Neurofilament Phosphorylation during Development and Disease: Which Came First, the Phosphorylation or the Accumulation? *J. Amino Acids.*

Delisle, M.B., & Carpenter, S. (1984). Neurofibrillary axonal swellings and amyotrophic lateral sclerosis. *J. Neurol. Sci.*

Dickson, T.C., King, C.E., McCormack, G.H., & Vickers, J.C. (1999). Neurochemical diversity of dystrophic neurites in the early and late stages of Alzheimer's disease. *Exp. Neurol.*

Fen-Biao Gao& Sandra Almeida, R.L. (2017). Dysregulated molecular pathways in amyotrophic lateral sclerosis–frontotemporal dementia spectrum disorder. *Embo J.*

Ferrari, R., Kapogiannis, D., D. Huey, E., & Momeni, P.,(2011). F*TD and ALS: A Tale of Two Diseases. Curr. Alzheimer Res. 8*, 273–294.

figure Papez circuit [WWW Document], n.d.

Filippini, N., Douaud, G., MacKay, C.E., Knight, S., Talbot, K., & Turner, M.R. (2010). Corpus callosum involvement is a consistent feature of amyotrophic lateral sclerosis. *Neurology, 75,* 1645–1652.

Garbern, J.Y., Yool, D.A., Moore, G.J., Wilds, I.B., Faulk, M.W., Klugmann, M., Nave, K.A., Sistermans, E.A., Van Der Knaap, M.S., Bird, T.D., Shy, M.E., Kamholz, J.A., & Griffiths, I.R. (2002). Patients lacking the major CNS myelin protein, proteolipid protein 1, develop length-dependent axonal degeneration in the absence of demyelination and inflammation. *Brain, 125*, 551–561.

Ghosh, S., Lippa, C.F. (2015). Clinical Subtypes of Frontotemporal Dementia. *Am. J. Alzheimers. Dis. Other Demen. 30,* 653–661.

Harsan, L.A., Poulet, P., Guignard, B., Steibel, J., Parizel, N., De Sousa, P.L., Boehm, N., Grucker, D., & Ghandour, M.S. (2006). Brain dysmyelination and recovery assessment by noninvasive in vivo diffusion tensor magnetic resonance imaging. *J. Neurosci. Res. 83,* 392–402.

Heinrich, M.P., Jenkinson, M., Bhushan, M., Matin, T., Gleeson, F. V., Brady, S.M., &Schnabel, J.A. (2012). MIND: Modality independent neighbourhood descriptor for multi-modal deformable registration. *Med. Image Anal.*

Henkel, J.S., Engelhardt, J.I., Sikls, L., Simpson, E.P., Kim, S.H., Pan, T., Goodman, J.C., Siddique, T., Beers, D.R., & Appel, S.H. (2004). Presence of Dendritic Cells, MCP-1, and Activated Microglia/Macrophages in Amyotrophic Lateral Sclerosis Spinal Cord Tissue. *Ann. Neurol. 55*, 221–235.

Hopwood, D., (1969). Fixatives and fixation: a review. *Histochem. J.*

Hornberger, M., & Piguet, O. (2012). Episodic memory in frontotemporal dementia: a critical review. *Brain 135,* 678–92.

Hornberger, M., Wong, S., Tan, R., Irish, M., Piguet, O., Kril, J., Hodges, J.R., & Halliday, G. (2012). In vivo and post-mortem memory circuit integrity in frontotemporal dementia and Alzheimer's disease. *Brain 135*, 3015–3025.

Horsfield, M.A., & Jones, D.K. (2002). Applications of diffusion-weighted and diffusion tensor MRI to white matter diseases - A review. *NMR Biomed.*

Hu, W.T., & Grossman, M. (2009). TDP-43 and frontotemporal dementia. *Curr. Neurol. Neurosci. Rep.*

Huszar IN, Miller KL, Pallebage-Gamarallage M, Ansorge O, & Mirfin C, H.M. (2018). Pipeline for registering histological sections to MRI volumes; *abstract ISMRM conference Paris., in: Pipeline for Registering Histological Sections to MRI Volumes.*

Hyman, B.T., Van Hoesen, G.W., Kromer, L.J., & Damasio, A.R. (1986). Perforant pathway changes and the memory impairment of Alzheimer's disease. *Ann. Neurol.*

Irish, M., Devenney, E., Wong, S., Dobson-Stone, C., Kwok, J.B., Piguet, O., Hodges, J.R., & Hornberger, M. (2013). Neural substrates of episodic memory dysfunction in behavioural variant frontotemporal dementia with and without C9ORF72 expansions. *NeuroImage Clin.*

Jbabdi, S., & Johansen-Berg, H. (2011). Tractography: Where Do We Go from Here? *Brain Connect. 1,* 169–183.

Jbabdi, S., Sotiropoulos, S.N., Haber, S.N., Van Essen, D.C., & Behrens, T.E. (2015). Measuring macroscopic brain connections in vivo. *Nature Neuroscience. 18*, 1546–1555.

Jbabdi, S., Sotiropoulos, S.N., Savio, A.M., Graña, M., & Behrens, T.E.J. (2012). Model-based analysis of multishell diffusion MR data for tractography: How to get over fitting problems. *Magn. Reson. Med. 68,* 1846–1855.

Kerschensteiner, M., Schwab, M.E., Lichtman, J.W., & Misgeld, T. (2005). In vivo imaging of axonal degeneration and regeneration in the injured spinal cord. *Nat. Med.*

Klawiter, E.C., Schmidt, R.E., Trinkaus, K., Liang, H.F., Budde, M.D., Naismith, R.T., Song, S.K., Cross, A.H., & Benzinger, T.L. (2011). Radial diffusivity predicts demyelination in ex vivo multiple sclerosis spinal cords. *Neuroimage, 55,* 1454–1460.

Larsen, L., Griffin, L.D., Gräßel, D., Witte, O.W., & Axer, H. (2007). Polarized light imaging of white matter architecture. *Microsc. Res. Tech. 70*, 851–863.

Lillo, P., Mioshi, E., Burrell, J.R., Kiernan, M.C., Hodges, J.R., Hornberger, & M. (2012). Grey and White Matter Changes across the Amyotrophic Lateral Sclerosis-Frontotemporal Dementia Continuum. *PLoS One, 7.*

Lingor, P., Koch, J.C., Tönges, L., & Bähr, M. (2012). Axonal degeneration as a therapeutic target in the CNS. *Cell Tissue Res.*

Logroscino, G., Traynor, B.J., Hardiman, O., Chio, A., Mitchell, D., Swingler, R.J., Millul, A., Benn, E., & Beghi, E. (2010). Incidence of amyotrophic lateral sclerosis in Europe. J. Neurol. Neurosurg. *Psychiatry, 81*, 385–390.

Mackenzie, I.R., & Rademakers, R. (2008). The role of transactive response DNA-binding protein-43 in amyotrophic lateral sclerosis and frontotemporal dementia. *Current Opinions in Neurology. 21,* 693–700.

Metwalli, N.S., Benatar, M., Nair, G., Usher, S., Hu, X., & Carew, J.D. (2010). Utility of axial and radial diffusivity from diffusion tensor MRI as markers of neurodegeneration in amyotrophic lateral sclerosis. *Brain Res. 1348,* 156–164.

Miller, K.L., Stagg, C.J., Douaud, G., Jbabdi, S., Smith, S.M., Behrens, T.E.J., Jenkinson, M., Chance, S.A., Esiri, M.M., Voets, N.L., Jenkinson, N., Aziz, T.Z., Turner, M.R., Johansen-Berg, H., & McNab, J.A. (2011). Diffusion imaging of whole, post-mortem human brains on a clinical MRI scanner. *Neuroimage, 57,* 167–181.

Mollink, J., Kleinnijenhuis, M., Cappellen van Walsum, A.M. van, Sotiropoulos, S.N., Cottaar, M., Mirfin, C., Heinrich, M.P., Jenkinson, M., Pallebage-Gamarallage, M., Ansorge, O., Jbabdi, S., & Miller, K.L. (2017). Evaluating fibre orientation dispersion in white matter: Comparison of diffusion MRI, histology and polarized light imaging. *Neuroimage.*

Montine, T.J., Phelps, C.H., Beach, T.G., Bigio, E.H., Cairns, N.J., Dickson, D.W., Duyckaerts, C., Frosch, M.P., Masliah, E., Mirra, S.S., Nelson, P.T., Schneider, J.A., Thal, D.R., Trojanowski, J.Q., Vinters, H. V., & Hyman, B.T. (2012). National institute on aging-Alzheimer's association guidelines for the neuropathologic assessment of Alzheimer's disease: A practical approach. *Acta Neuropathol. 123,* 1–11.

Pessoa, L., & Hof, P.R. (2015). From Paul Broca's great limbic lobe to the limbic system. J. *Comp. Neurol.*

Phukan, J., Elamin, M., Bede, P., Jordan, N., Gallagher, L., Byrne, S., Lynch, C., Pender, N., & Hardiman, O.(2012). The syndrome of cognitive impairment in amyotrophic lateral sclerosis: a population-based study. J. Neurol. Neurosurg. *Psychiatry, 83*, 102–8.

Schmierer, K., Wheeler-Kingshott, C.A.M., Boulby, P.A., Scaravilli, F., Altmann, D.R., Barker, G.J., Tofts, P.S., & Miller, D.H. (2007). Diffusion tensor imaging of post mortem multiple sclerosis brain. *Neuroimage, 35,* 467–477.

Schmierer, K., Wheeler-Kingshott, C.A.M., Tozer, D.J., Boulby, P.A., Parkes, H.G., Yousry, T.A., Scaravilli, F., Barker, G.J., Tofts, P.S., & Miller, D.H. (2008). Quantitative magnetic resonance of postmortem multiple sclerosis brain before and after fixation. 268–277.

Scotter, E.L., Chen, H.J., & Shaw, C.E. (2015). TDP-43 Proteinopathy and ALS: Insights into Disease Mechanisms and Therapeutic Targets. *Neurotherapeutics.*

Shah, A., Jhawar, S.S., & Goel, A. (2012). Analysis of the anatomy of the Papez circuit and adjoining limbic system by fiber dissection techniques. *Journal of Clininacal Neuroscience 19,* 289–298.

Shepherd, T.M., Thelwall, P.E., Stanisz, G.J., & Blackband, S.J.(2009). Aldehyde fixative solutions alter the water relaxation and diffusion properties of nervous tissue. *Magn. Reson. Med. 62*, 26–34.

Soares, J.M., Marques, P., Alves, V., & Sousa, N., (2013). A hitchhiker's guide to diffusion tensor imaging. *Frontiers in Neurosciense.*

Song, S.K., Sun, S.W., Ramsbottom, M.J., Chang, C., Russell, J., & Cross, A.H. (2002). Dysmyelination revealed through MRI as increased radial (but unchanged axial) diffusion of water. *Neuroimage, 17*, 1429–1436.

Sparkman, N.L., & Johnson, R.W. (2008). Neuroinflammation associated with aging sensitizes the brain to the effects of infection or stress. *Neuroimmunomodulation.*

Sreedharan, J., Blair, I.P., Tripathi, V.B., Hu, X., Vance, C., Rogelj, B., Ackerley, S., Durnall, J.C., Williams, K.L., Buratti, E., Baralle, F., de Belleroche, J., Mitchell, J.D., Leigh, P.N., Al-Chalabi, A., Miller, C.C., Nicholson, G., & Shaw, C.E.(2008). TDP-43 mutations in familial and sporadic amyotrophic lateral sclerosis. *Science, 319,* 1668–72.

Sugiyama, M., Takao, M., Hatsuta, H., Funabe, S., Ito, S., Obi, T., Tanaka, F., Kuroiwa, Y., & Murayama, S. (2013). Increased number of astrocytes and macrophages/microglial cells in the corpus callosum in amyotrophic lateral sclerosis. *Neuropathology, 33*, 591–599.

Sun, S.W., Liang, H.F., Xie, M., Oyoyo, U., & Lee, A. (2009). Fixation, not death, reduces sensitivity of DTI in detecting optic nerve damage. *Neuroimage, 44*, 611–619.

Sun, S.W., Neil, J.J., Liang, H.F., He, Y.Y., Schmidt, R.E., Hsu, C.Y., & Song, S.K. (2005). Formalin fixation alters water diffusion coefficient magnitude but not anisotropy in infarcted brain. *Magn. Reson. Med., 53*, 1447–1451.

Taddei-Ferretti C. Musio, (1997). Neuronal Bases and Psychological Aspects of Consciousness.

Takeda, T., Uchihara, T., Mochizuki, Y., Mizutani, T., & Iwata, M. (2007). Memory deficits in amyotrophic lateral sclerosis patients with dementia and degeneration of the perforant pathway A clinicopathological study. *Journal of Neurological Science, 260,* 225–230.

Takeda, T., Uchihara, T., Mochizuki, Y., Mizutani, T., & Iwata, M. (2007). Memory deficits in amyotrophic lateral sclerosis patients with dementia and degeneration of the perforant pathway. A clinicopathological study. *Journal of Neurological Science. 260,* 225–230.

Tan, R.H., Ke, Y.D., Ittner, L.M., & Halliday, G.M. (2017). ALS/FTLD: experimental models and reality. *Acta Neuropathol.*

Tan, R.H., Kril, J.J., Fatima, M., McGeachie, A., McCann, H., Shepherd, C., Forrest, S.L., Affleck, A., Kwok, J.B.J., Hodges, J.R., Kiernan, M.C., & Halliday, G.M. (2015). TDP-43 proteinopathies: Pathological identification of brain regions differentiating clinical phenotypes. *Brain, 138*, 3110–3122.

Thal, D.R., Holzer, M., Rüb, U., Waldmann, G., Günzel, S., Zedlick, D., & Schober, R. (2000). Alzheimer-related τ-pathology in the perforant path target zone and in the hippocampal stratum oriens and radiatum correlates with onset and degree of dementia. *Experimental Neurology.*

Thavarajah, R., Mudimbaimannar, V., Rao, U., Ranganathan, K., & Elizabeth, J. (2012). Chemical and physical basics of routine formaldehyde fixation. *J. Oral Maxillofac. Pathol. 16,* 400.

Thivard, L., Pradat, P.-F., Lehéricy, S., Lacomblez, L., Dormont, D., Chiras, J., Benali, H., & Meininger, V. (2007). Diffusion tensor imaging and voxel based morphometry study in amyotrophic lateral sclerosis: relationships with motor disability. *J. Neurol. Neurosurg. Psychiatry, 78,* 889–92.

Tyszka, J.M., Readhead, C., Bearer, E.L., Pautler, R.G., & Jacobs, R.E. (2006). Statistical diffusion tensor histology reveals regional dysmyelination effects in the shiverer mouse mutant. *Neuroimage, 29,* 1058–1065.

Waller, A. (1850). Experiments on the Section of the Glossopharyngeal and Hypoglossal Nerves of the Frog, and Observations of the Alterations Produced Thereby in the Structure of Their Primitive Fibres. *Philos. Trans. R. Soc. London.*

Warren, J.D., Rohrer, J.D., Rossor, & M.N. (2013). Clinical review. Frontotemporal dementia. *BMJ, 347*, f4827.

Werner, M., Chott, A., Fabiano, A., & Battifora, H. (2000). Effect of formalin tissue fixation and processing on immunohistochemistry. *Am. J. Surg. Pathol. 24,* 1016–1019.

Woolrich, M.W., Jbabdi, S., Patenaude, B., Chappell, M., Makni, S., Behrens, T., Beckmann, C., Jenkinson, M., & Smith, S.M. (2009). Bayesian analysis of neuroimaging data in FSL. *Neuroimage.*